JGR Oceans

RESEARCH ARTICLE
10.1029/2022JC019477

Key Points:

- The land breeze system amplitude and geographical coverage in the Bay of Bengal is maximum in July–August and minimum in December–January
- A well-defined diurnal variation in latent heat flux and near-surface current variability is associated with the land breeze system
- Differential heating between ocean and land leads to land breeze, though the prevailing large-scale winds determine its offshore extension

Supporting Information:

Supporting Information may be found in the online version of this article.

Correspondence to:

M. S. Girishkumar,
girish@incois.gov.in

Citation:

Athulya, K., Girishkumar, M. S., McPhaden, M. J., & Kolukula, S. S. (2023). Seasonal variation of the land breeze system in the southwestern Bay of Bengal and its influence on air-sea interactions. *Journal of Geophysical Research: Oceans*, *128*, e2022JC019477. https://doi.org/10.1029/2022JC019477

Received 10 NOV 2022
Accepted 13 JAN 2023

Author Contributions:

Conceptualization: M. S. Girishkumar
Data curation: S. S. Kolukula
Formal analysis: K. Athulya, M. S. Girishkumar, M. J. McPhaden
Investigation: M. S. Girishkumar
Methodology: K. Athulya, M. S. Girishkumar, M. J. McPhaden
Supervision: M. S. Girishkumar, M. J. McPhaden
Writing – original draft: M. S. Girishkumar
Writing – review & editing: K. Athulya, M. S. Girishkumar, M. J. McPhaden

Seasonal Variation of the Land Breeze System in the Southwestern Bay of Bengal and Its Influence on Air-Sea Interactions

K. Athulya[1,2], M. S. Girishkumar[1], M. J. McPhaden[3], and S. S. Kolukula[1]

[1]Ministry of Earth Sciences (MoES), Indian National Centre for Ocean Information Services (INCOIS), Hyderbad, India, [2]School of Ocean Science and Technology, Kerala University of Fisheries and Ocean Studies, Cochin, India, [3]NOAA/Pacific Marine Environmental Laboratory, Seattle, WA, USA

Abstract This study examines the seasonal variability of the Land Breeze System (LBS) in the Bay of Bengal (BoB) using hourly moored buoy data, coastal radar data, atmospheric reanalysis data, and 6-hourly satellite-based Cross-Calibrated Multi-Platform (CCMP) wind velocity data. We first provide an overview of the LBS for the entire BoB, then focus on the pronounced LBS in southwestern BoB and its impact on the near-surface current field and latent heat flux (LHF). We show that the LBS in the southwestern BoB exhibits a maximum diurnal wind speed amplitude of ∼2 m s^{-1} with seaward nearshore winds best developed in the morning hours. The geographical coverage is maximum in July and August and minimum in December and January. During its peak phase in July–August, the signature of the LBS in the southwestern BoB extends up to 600 km offshore, occupies ∼20% of the basin, and accounts for approximately 15% of the seasonal mean wind speed variance. The near-surface current field shows a rapid response to the diurnal wind speed variations, with an eastward current observed between 1000–1800 IST, a westward current between 1800–0800 IST, and a diurnal range of 12 cm s^{-1}. LHF shows well-defined diurnal variability in response to diurnal LBS wind speed variability, with a morning maximum, evening minimum, and a diurnal range of 35 W m^{-2}. We also find that the large-scale seasonal winds are the main factor in determining the annual variability in strength and geographical coverage of the LBS in the southwestern BoB.

Plain Language Summary The land-sea breeze system that occurs due to differential heating between the land and ocean surfaces is a vital component of the climate system. In this study, we examine the seasonality of the land breeze signal and associated air-sea interaction processes in the southwestern Bay of Bengal (BoB) using moored buoy measurements together with reanalysis, satellite, and coastal radar data. As a result of seasonally evolving large-scale winds, which are offshore during boreal summer and onshore during boreal winter, the land breeze signal in the southwestern BoB shows an annual variability with maximum amplitude and geographical coverage during July and August and a minimum during December and January. During its summer peak phase, the signature of the land breeze signal is evident up to 600 km offshore from the coastal region in the southwestern BoB. Modulation of wind speed due to the land breeze signal also results in a well-defined diurnal variability in latent heat flux and near-surface current variability.

1. Introduction

Sea surface temperature (SST) in the Bay of Bengal (BoB) plays a vital role in determining the spatio-temporal variability of Indian summer monsoon precipitation (Jiang & Li, 2011; Samanta et al., 2018; Shenoi et al., 2002). Due to the persistent occurrence of the relatively thin salt-stratified mixed layers, primarily owing to a large influx of freshwater from intense precipitation and continental rivers (Girishkumar et al., 2011; Rao and Sivakumar, 2003; Shetye et al., 1996; Thadathil et al., 2007), SST in the BoB is highly sensitive to surface fluxes (Duncan & Han, 2009). Moreover, the SST in the BoB is always higher than 28°C (Shenoi et al., 2002), a favorable condition for the formation of deep convection in the tropics. Due to the high mean SST, a small change in its magnitude can significantly feedback to the overlying atmosphere so as to influence the amplitude of intraseasonal and interannual signals over the BoB. Hence, it is imperative to understand the processes affecting air-sea fluxes that modulate SST in the BoB on different temporal scales to better represent ocean-atmosphere interactions in weather and climate forecast models.

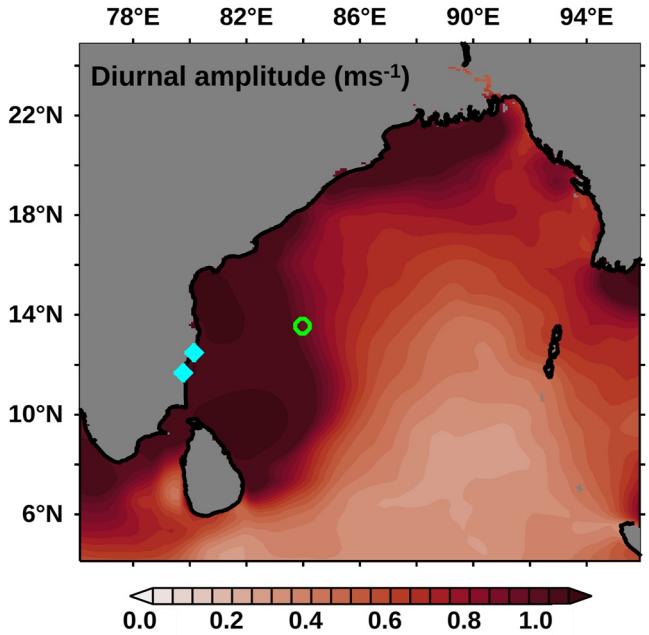

Figure 1. Annual average of diurnal amplitude of Cross-Calibrated Multi-Platform 6-hourly wind speed (m s^{-1}) estimated based on data from 1 January 2010–31 December 2019. The green circle represents the location of open ocean buoy BD11 at 13.5°N, 84.0°E in the southwestern Bay of Bengal, and the cyan diamond symbols represent the location of high frequency radar stations (11.7°N, 79.8°E, and 12.5°N, and 80.2°E). The diurnal amplitude values are significantly different from zero at the 99% confidence level at every grid point based on the application of a *t*-test.

There have been many previous attempts to document air-sea interaction processes in the BoB that are important of weather and climate (Bhat & Fernando, 2016; Bhat et al., 2001; Cyriac et al., 2016; Dey et al., 2017; Girishkumar et al., 2011, 2017; Joseph et al., 2021; Prasad, 2004; Praveen Kumar et al., 2017; Rao and Sivakumar, 2000; Sengupta and Ravichandran, 2001; Shenoi et al., 2002; Srivastava et al., 2018; Thangaprakash et al., 2016; Webster et al., 2002; Weller et al., 2016, 2019; Yu et al., 2007). These studies helped to advance our knowledge of variability across a broad range of phenomena spanning intraseasonal to decadal time scales. Air-sea interaction processes on sub-daily timescale are also essential to understanding the climate system. For example, based on a one-dimensional mixed layer model, Bernie et al. (2005) and Mujumdar et al. (2011) demonstrated that forcing a numerical model with fluxes that resolve sub-daily variations is essential to reproduce the amplitude of intraseasonal SST variability realistically. However, the knowledge of air-sea interaction processes on a sub-daily time scale in the BoB is poor, primarily due to the historically limited availability of high temporal resolution time series measurements of near-surface meteorological and oceanographic parameters. However, with the advent of the Research Moored Array for African-Asian-Australian Monsoon Analysis and Prediction (RAMA) (McPhaden et al., 2009) and the Ocean Moored buoy Network for the Northern Indian Ocean (OMNI) (Venkatesan et al., 2013), the availability of such data has greatly increased. The possibility now exists to explore processes at work on very short time scales in novel and unique ways. For example, based on the measurements from three RAMA moorings in the central BoB, Joseph et al. (2021) and Girishkumar et al. (2021) examined sub-daily variability of atmospheric cold pool events and their effects on surface heat fluxes and SST. In addition, Turk et al. (2021) and Giglio et al. (2022) used moored buoy observations to document sub-daily wind speed variability in open ocean regions of the tropics.

The land-sea breeze system that occurs due to differential heating between the land and ocean surfaces evolves over the course of a day and is a vital component of the climate system at least in coastal regions (Stull, 1988). During the daytime, the land heats up faster than the surrounding ocean. A pressure gradient develops that is directed towards land, leading to the formation of onshore winds referred to as a sea breeze. During nighttime, land cools relatively fast, but the ocean surface takes more time to cool owing to its higher heat capacity. A pressure gradient directed towards the ocean develops, leading to winds blowing offshore referred to as a land breeze. These onshore (sea breeze) and offshore (land breeze) winds together constitute the land-sea breeze system (Wexler, 1946).

The land-sea breeze system plays a vital role in determining regional climate (M. Aparna et al., 2005; Chen et al., 2016; Clancy et al., 1979; Davis et al., 2019; Hamza & Babu, 2007; Hill et al., 2010; Kilpatrick et al., 2017 Miller et al., 2003; Pielke, 1973; Rani et al., 2010; Short et al., 2019; Woodson et al., 2007; Zhu et al., 2017). Many studies of the land-sea breeze system, as reviewed by Miller et al. (2003), focused mainly on the impact of the sea breeze on inland fetches. However, the impact of the Land Breeze System (LBS) on offshore regions has received relatively little attention because of the aforementioned limited availability of in-situ data. However, a few studies have examined the impact of the LBS on different parts of the global ocean. Neetu et al. (2006) studied the impact of the LBS on ocean surface waves over the eastern Arabian Sea and Rafiq et al. (2020) studied the impact of the LBS on coastal currents of the southwestern Australian coast. Based on moored buoy observation in the Red Sea, Davis et al. (2019) have shown that the LBS has the potential to modulate local air-sea interaction processes. Using multi-mission scatterometer data, Gille et al. (2003, 2005) provided a global view of diurnal wind variations associated with land and sea breezes. Their study further demonstrated the existence of an LBS in the southwestern BoB, but did not evaluate the seasonality of the LBS or its impact on air-sea interaction processes.

In this study, we take advantage of near-surface meteorological and oceanographic parameters with one-hour temporal resolution from a moored buoy in the open ocean at 13.5°N, 84.0°E in the southwestern BoB (Figure 1),

Table 1
Sensor Specification of BD11 Mooring

Parameters	Sensor type	Make/model	Accuracy
Wind speed	Cup anemometer	Lambrecht/1453	±2%
Wind direction	Vane + flux gate compass	Lambrecht/1453	1.5–4°
Air temperature	Pt/100 RTD	Rotronic/MP 102A	±0.3°C
Relative humidity	Capacitance		±1%
Downwelling long-wave radiation	Pyrgeometer	Eppley/PIR	5%
Downwelling short-wave	Pyranometer	Eppley/PSP	3%
Water temperature	Thermistor	Seabird/Micro-CAT SBE37	0.002°C
Single point	Doppler volume sampler	Teledyne RD Instrument 150 kHZ	Velocity: ±1% Dir: ±2°

satellite-based Cross-Calibrated Multi-Platform (CCMP) wind velocity data, coastal radar data and the European Centre for Medium-Range Weather Forecasts (ECMWF) reanalysis (ERA5) product to address the following questions:

1. What is the seasonality of the LBS in the BoB?
2. What causative mechanisms are responsible for the seasonality of LBS in the BoB?
3. What is the impact of the LBS on the near-surface current field in the southwestern BoB?
4. What is the impact of the LBS on latent heat flux (LHF) in the southwestern BoB?

The present study is organized as follows. The data set used and the methodology followed are summarized in Section 2. Seasonal variability in the diurnal amplitude of the LBS and its impact on air-sea interaction processes are described in Section 3. Finally, key results are summarized in Section 4.

2. Data and Methods

The near-surface meteorological and oceanographic measurements with a temporal resolution of 1 hr from the mooring located at 13.5°N, 84.0°E (designated BD11) are used in the present study (Venkatesan et al., 2013). The temperature data at 1 m water depth from BD11 is used as a proxy for SST. The mooring measures humidity and air temperature at 3 m above the sea surface, downwelling longwave and downwelling shortwave radiation, wind speed at 4 m height, and ocean current velocity using a doppler volume current sampler (DVS) at a depth of 1.5 m depth.

LHF is estimated from mooring SST, humidity, wind speed, downwelling shortwave, and downwelling longwave radiation using the Coupled Ocean-Atmosphere Response Experiment (COARE) bulk flux algorithm version 3.6 with diurnal warm-layer and cool skin correction (Edson et al., 2013; Fairall et al., 1996, 2003). Downwelling longwave radiation data from the mooring were in error during the study period, so that downwelling longwave radiation data from Clouds and the Earth's Radiant Energy System (CERES) with 1° × 1° spatial resolution and one-hour temporal resolution (Wielicki et al., 1996) were used instead to estimate LHF from the bulk algorithm. A comparison of downwelling longwave radiation data from CERES with measurements from RAMA buoys at 15°N, 90°E in the central BoB and 5°N, 95°E in the eastern equatorial Indian Ocean demonstrated that CERES data were a reasonable replacement for missing in-situ data at BD11 (A. R. Aparna & Girishkumar, 2022; Girishkumar et al., 2021; Joseph et al., 2021). BD11 also measures sub-surface temperature and salinity though these data are not used in the present study. Specifications of BD11 sensors are summarized in Table 1, and data availability from the mooring is presented in Figure 2.

The measurements from the BD11 mooring have a sufficient temporal resolution to resolve the LBS in the southwestern BoB. For instance, a week-long time series of wind speed derived from BD11 during 22–29 July 2017 shows well-defined sub-daily variability with a diurnal range of 2 m s^{-1} in the wind speed (Figure 3c; blue line). These features are the primary focus of the present study.

In addition to moored buoy data, the spatio-temporal variability of LBS in the BoB is evaluated using CCMP 6-hourly gridded surface wind vectors data with 0.25° spatial resolution (Wentz et al., 2015). The CCMP wind data from 2010 to 2019 are subjected to Fast Fourier transform (FFT) analysis to estimate the diurnal amplitude

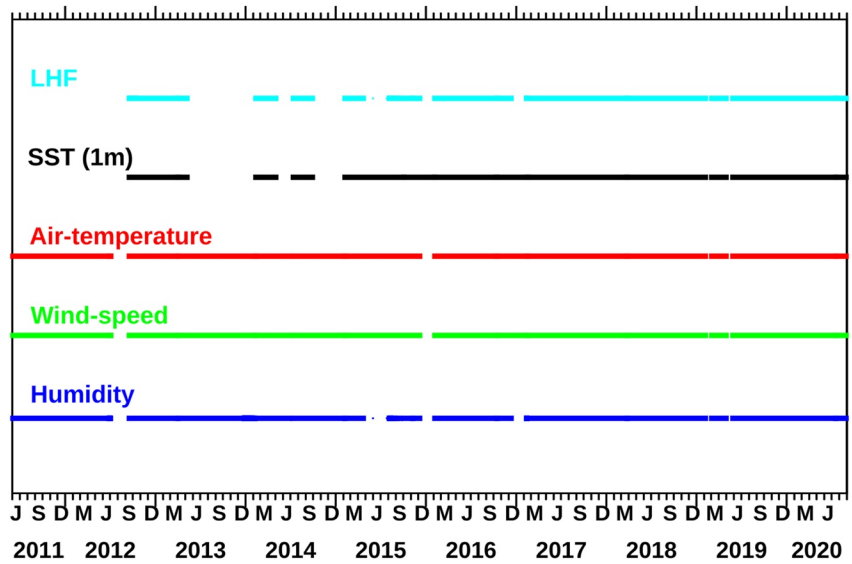

Figure 2. Data availability of near-surface meteorological and oceanographic parameters relative humidity (blue), wind speed (green), air temperature (red), sea surface temperature (black), and latent heat flux (cyan), from the open ocean buoy BD11 at 13.5°N and 84.0°E in the southwestern Bay of Bengal.

of wind speed. To understand the monthly evolution of diurnal wind speed amplitude, the diurnal amplitude of wind speed of every month is estimated separately during 2010 and 2019, and its average value is calculated to form a climatology. This approach is similar to previous studies that analyzed the annual modulation of the diurnal cycle in surface winds (Gille et al., 2005; Ueyama and Deser, 2008). An alternative approach to FFT for estimating the diurnal LBS winds would be to use a least squares fit to harmonics as in Giglio et al. (2022). However, they found that harmonic fits slightly underestimate the amplitude of the diurnal signal compared to using an FFT approach. Thus, for this reason and because of its simplicity, we prefer to use FFT to define the diurnal amplitude of wind speed.

To understand the large-scale impact of the LBS in the southwestern BoB, we use hourly air temperature, relative humidity, and wind velocity from the ECMWF ERA5 reanalysis with a spatial resolution of 25 km (Hersbach et al., 2020). We note that the CCMP wind analysis product finds a solution using the Variational Analysis Method (VAM) that best fits the data from satellites, moored buoys observation, and wind field from ERA-Interim reanalysis product as a first-guess. Moreover, ERA5 assimilates buoy data, including BD11. Hence, BD11, CCMP, and ERA5 are not completely independent of one another. However, CCMP and ERA use different analysis methods, so the use of the different products helps to build confidence in our results.

Ocean surface current vectors derived from a pair (separated by ∼100 km) of high frequency (HF) radars installed at the southeastern coast of India (11.7°N, 79.8°E, and 12.5°N and 80.2°E) are also used to describe surface current variability in the southwestern BoB (Jena et al., 2019) (Figure 1; cyan diamonds). The HF radar operating frequency is 4.4 MHz and can provide surface current measurements as far as 200 km from the coast at a spatial resolution of 6 km and a temporal resolution of 1 hr (Jena et al., 2019). Due to variations in the roughness of the sea surface and electromagnetic interference from environmental sources, the HF radar measurements have spatial data gaps. Thus, we used a HF radar current product with gaps filled by a complex empirical orthogonal method (Kolukula et al., 2020).

All the analyses were presented in Indian Standard Time (IST; 5h 30 min ahead of UTC). The offset between the local time and IST at the BD11 location (84°E) is 6 min, and the eastern boundary of the southwest coast of the BoB (80.5°E) is around 4 min. The daily mean (0600–0500 IST) of meteorological parameters on a particular day is removed to estimate the daily anomaly field. The LSB system is primarily determined by differential heating between land and ocean, which is crucially dependent on the diurnal cycle of insolation. The mean sunrise time in the study region is around 0600 IST; hence, a 24-hr interval starting from 0600 IST defines 1 day in this study. This approach is similar to previous studies of sub-daily variability in the BoB (Jofia et al., 2021; Girishkumar et al., 2021) and the western equatorial Indian Ocean (Seo et al., 2014). The analysis is not sensitive to the precise

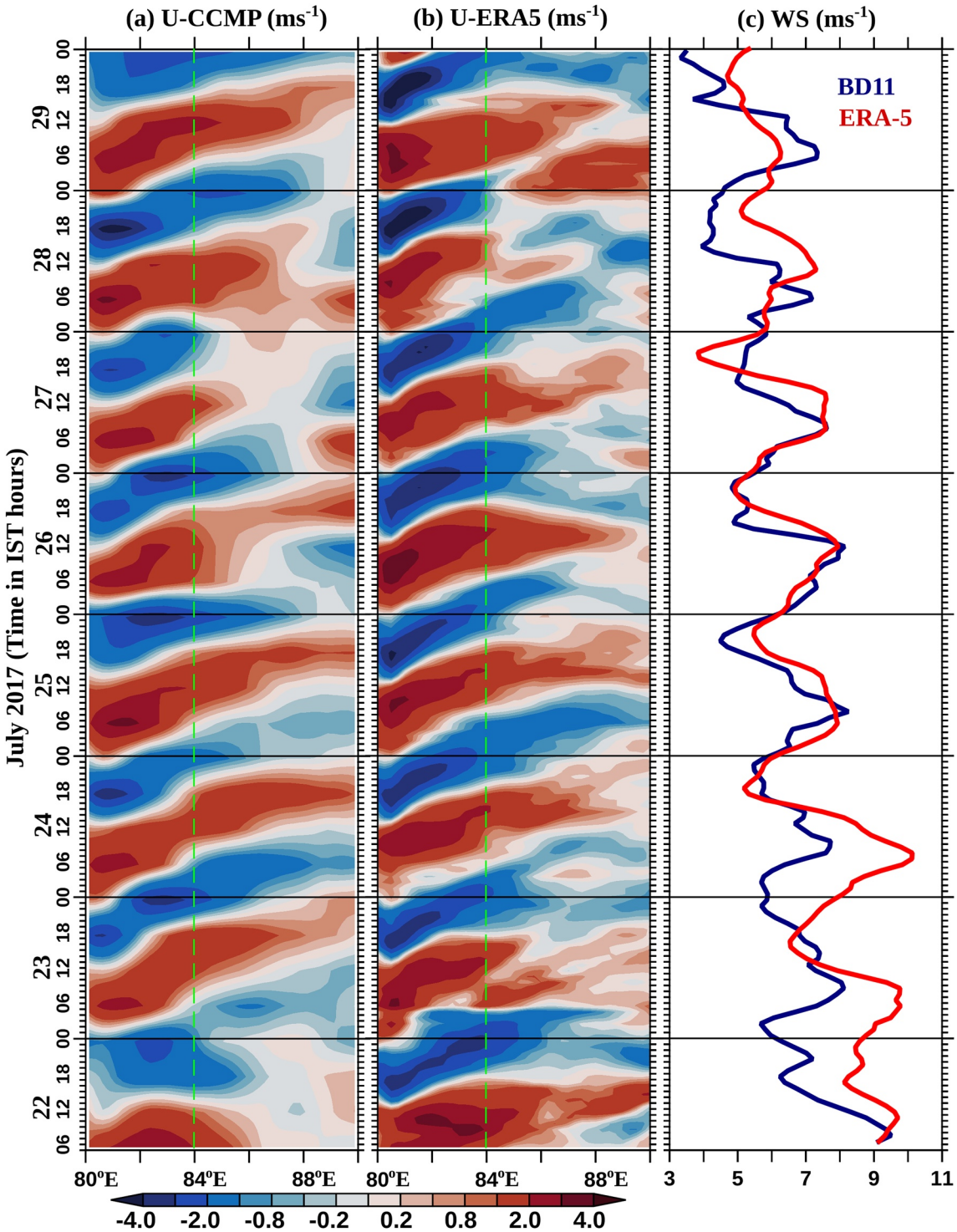

Figure 3. Temporal evolution as a function of longitudinal for (a) Cross-Calibrated Multi-Platform 6 hourly zonal wind speed anomaly (U; m s^{-1}), (b) ERA5 hourly zonal wind speed anomaly (U; m s^{-1}), and (c) wind speed (WS; m s^{-1}) derived from BD11 (blue) and ERA5 (red) at the same location as the buoy (13.5°N, 84.0°E) in the southwestern Bay of Bengal during 22–29 July 2017. The longitude (84.0°E) corresponding to the BD11 location is marked as green dashed vertical lines in panels (a) and (b). WS = $\sqrt{U^2 + V^2}$ based on the highest temporal resolution data.Time in IST hours.

Table 2
The Number of Days Considered for Deriving a Diurnal Composite for Various Parameters

Platform	Parameters	Period	Number of days
CCMP	Wind vectors	July–August (2010–2019)	620
BD11	Wind vectors	July–August (2011–2020)	411
	Current vectors		480
	Specific humidity		410
ERA5	LHF, wind speed vectors, air temperature	July–August (2010–2020)	682
HF radar	Current vectors	July–August (2010–2021)	409

definition of what constitutes a day, for example, using 0000–2300 IST instead of 0600–0500 IST does not significantly affect our results.

For ease of discussion, we mainly concentrate on the composite of sub-daily evolution of meteorological and oceanographic parameters. The number of days used to estimate the composite field for each parameter is summarized in Table 2. The statistical uncertainty of each parameter is presented as the one-standard error, estimated based on deviations from the respective means. The difference between the maximum and minimum value of a parameter in a day is defined as its diurnal amplitude.

The relative contribution of sub-daily variability of wind speed and air-sea specific humidity differences (Δq) on the sub-daily variability of LHF is examined by isolating their impact from one another. For this purpose, LHF is estimated by retaining only the sub-daily variability of wind speed (LHF_WS) while holding Δq to its daily mean; or by keeping only the sub-daily variability of air-sea specific humidity difference (LHF_Δq) while fixing wind speed to its daily mean.

3. Results and Discussion

3.1. Seasonal Variability of the LBS in the BoB

The annual average of FFT analysis of six-hourly CCMP wind speed data from 2010 to 2019 shows the geographic locations in the BoB where the most prominent diurnal variability persists (Figure 1). The diurnal wind speed amplitude shows its largest magnitude, with a maximum value (~1.5 m s^{-1}), in the southwestern BoB (Figure 1). This particular characteristic is consistent with Gille et al.'s (2005) analysis of four-times daily scatterometer wind observations, which they attributed to the LBS. A faint patch of diurnal wind speed amplitude is also apparent in the northwestern and eastern BoB, though the geographical coverage and magnitude are much smaller than the signature in the southwestern BoB.

The monthly evolution of the diurnal wind speed amplitude was evaluated to understand the seasonal variability in intensity and geographical spread of the LBS in the BoB (Figure 4a). The magnitude and spatial spread of wind speed's diurnal amplitude indicate a well-defined annual variability in the southwestern BoB (between 10.0°N and 16.0°N; 80.0°E and 84.0°E; marked as blue boxes in each panel of Figure 4a). Relatively low values in the diurnal amplitude of wind speed are evident between November and March (~0.8 m s^{-1}) during the Northeast Monsoon, followed by a sudden amplitude increase in May (Figure 4b; blue line). Peak intensity is reached during the Southwest Monsoon in July–August (~1.8 m s^{-1}), falling off from September onward and reaching a minimum value by December and January (Figure 4b; blue line). Between November and February, when the magnitude of the diurnal amplitude of wind speed is smallest, its spatial extent is apparent only as a narrow band in the coastal region of the southwestern BoB (Figure 4a). The geographical coverage of diurnal wind speed amplitude becomes noticeable over a much larger area between March and May, attaining maximum spatial coverage between July and August before decreasing afterward (Figure 4a). During July and August, the well-defined maxima in diurnal wind speed amplitude observed in the southwestern BoB exhibits maximum geographic extent covering approximately 20% of the entire BoB (blue box in Figure 4a). The amplitude of diurnal wind speed explains approximately 15% of the magnitude of total wind speed variability during July and August (Figure 4b; blue dashed line). These characteristics suggest that the diurnal variability of the wind speed associated with LBS in the southwestern BoB is a significant large-scale feature during the summer. In contrast,

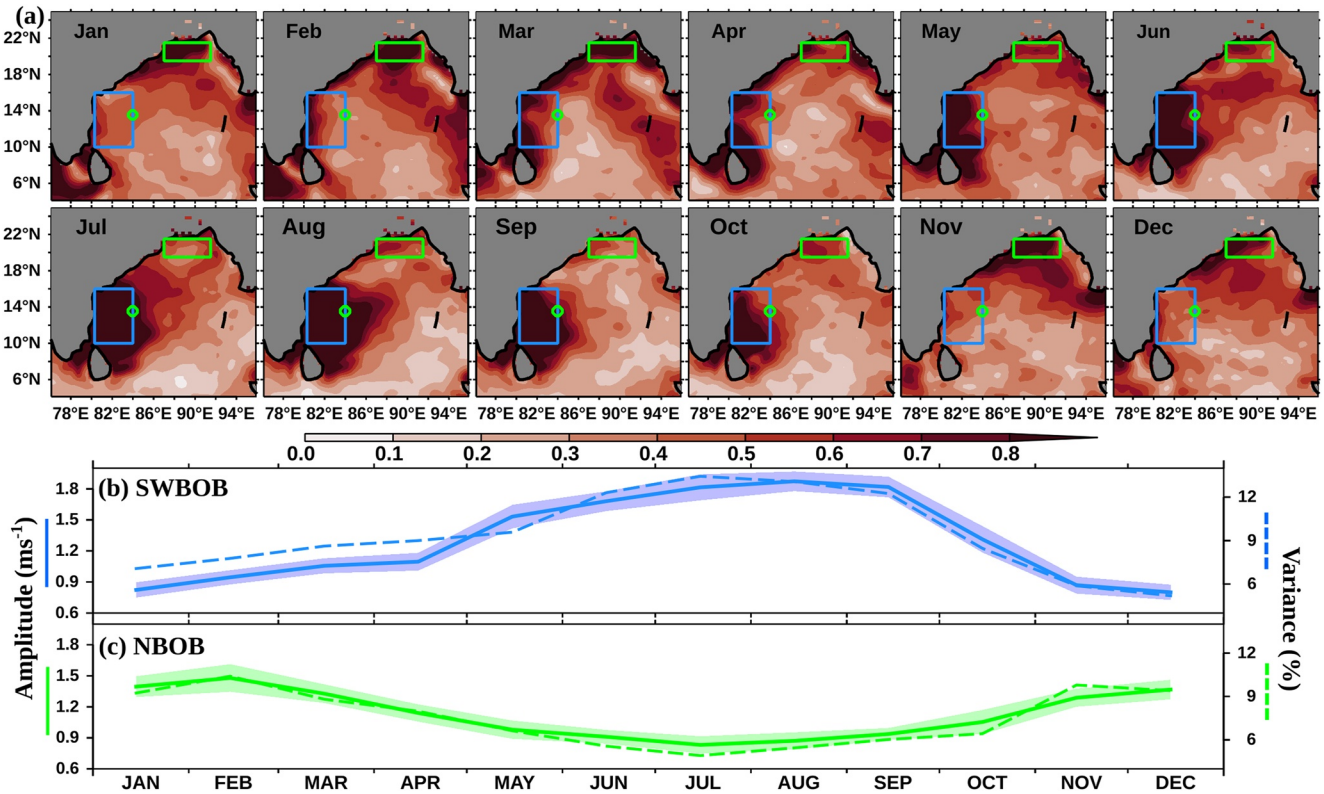

Figure 4. (a) Monthly evolution of the multi-year average (2010–2019) of the diurnal amplitude of wind speed (m s^{-1}) derived from 6-hourly Cross-Calibrated Multi-Platform (CCMP) data. (b) Temporal evolution of the diurnal amplitude of CCMP wind speed (left axis; blue line) and its percentage of the variance to the total wind speed (right axis; blue dashed line) averaged over 10.0°N–16.0°N and 80.0°E–84.0°E in the southwestern Bay of Bengal (BoB) (marked as a blue box in each panel of (a)). (c) Temporal evolution of the diurnal amplitude of CCMP wind speed (left axis; green line) and its percentage of the variance to the total wind speed (right axis; green dashed line) averaged over 19.5°N–21.5°N and 87.0°E–91.5°E in the northern BoB (marked as a green box in each panel of (a)). In (b) and (c), the shading represents the standard error of the mean estimated from the standard deviation for each monthly mean. The green circles in (a) represent the locations of mooring BD11 at 13.5°N, 84.0°E.

the diurnal wind speed contribution to the total wind speed variability is only 5%, or approximately a factor of three smaller, from November to March compared to July–August (Figure 4b; blue dashed lines).

The annual variability of the diurnal amplitude of wind speed in the northern BoB (green box in Figure 4a) shows roughly a mirror image compared to the evolution in the southwestern BoB (blue line Figure 4b and green line in Figure 4c). Relatively low values in the diurnal amplitude of wind speed are evident between June and August (~0.8 m s^{-1}) in the northern BoB, followed by a gradual increase in amplitude between September and October. Peak intensity is reached in November–February (~1.6 m s^{-1}), falling off from March onward and reaching a minimum value by July (Figure 4c; green line). During its peak phase between November and February, the amplitude of diurnal wind speed explains approximately 10% of the magnitude of total wind speed variability in the northern BoB (Figure 4c; green dashed line). However, the geographical coverage of the LBS signature in the northern BoB is restricted to a much smaller region than its counterpart in the southwestern BoB (Figure 4a).

3.2. Mechanisms Responsible for the Seasonally Varying Offshore Extension of the LBS in the BoB

In this section, we explore possible causative factors determining the seasonality in intensity and offshore spread of the LBS in the BoB. Previous studies reported that the magnitude of the cross-shore potential air temperature difference between land (T_L) and ocean (T_O), that is, ($\Delta T_{L\text{-}O}$), is the primary factor that determines the strength of the LBS (Masselink and Pattiaratchi, 2001; Miller and Keim, 2003; Rafiq et al., 2020). In particular, a lower surface temperature over the land would favor a stronger land breeze, and a higher temperature would favor a sea breeze. Wermter et al. (2022) demonstrated that a modification of atmosphere temperature above 2 m over the ocean and land would not have much impact on the onset time of the sea breeze/land breeze system, but these

features can significantly influence the strength and offshore geographical coverage of LBS. In addition, the prevailing large-scale wind speed direction is also an essential factor in determining the offshore extension of LBS (Masselink and Pattiaratchi, 2001; Miller and Keim, 2003; Rafiq et al., 2020). For example, a strong opposing (toward land) prevailing large-scale wind can reduce the offshore extension of the LBS.

Starting first with the southwestern BoB, the monthly evolution of the average minimum value in the difference between T_L (over the region 10.0°N–15.0°N; 78.0°E–80.0°E) and T_O (over 10.0°N–15.0°N; 80.0°E–82.0°E) during the night ($\Delta T_{L\text{-}O\_MN}$) shows well-defined annual variability (Figure 5d; blue line; refer Figure 6a for definitions). The annual cycle of $\Delta T_{L\text{-}O\_MN}$ shows a maximum negative value (~−6°C) from November to

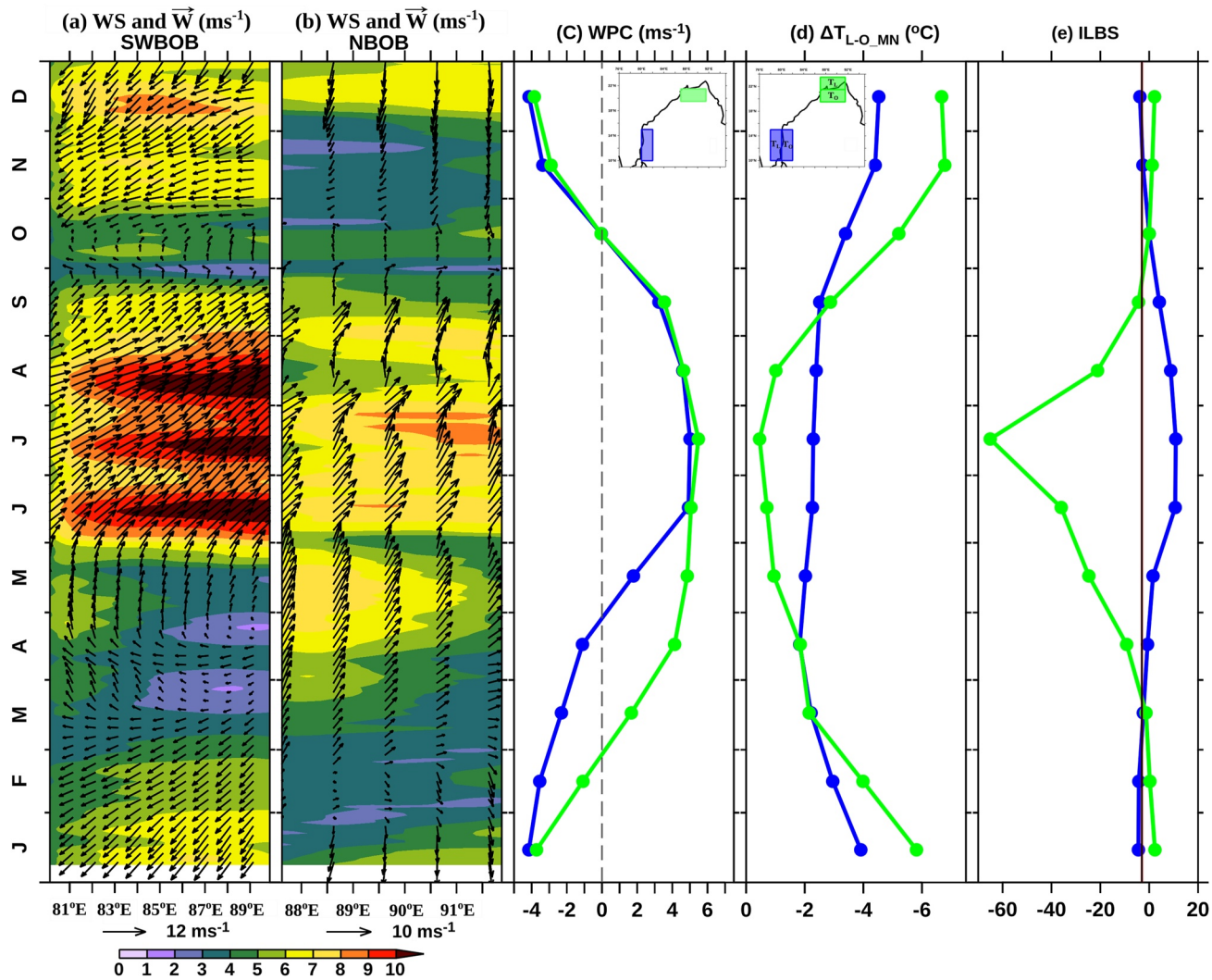

Figure 5. Monthly climatology (based on 2010–2019) of (a) Cross-Calibrated Multi-Platform (CCMP) wind speed (WS; m s^{-1}) and vectors ($\overrightarrow{W}$; m s^{-1}) averaged over the latitude band 10.0°N–15.0°N in the southwestern Bay of Bengal (BoB), (b) CCMP wind speed and vectors averaged over the latitude band 19.5°N–21.5°N in the northern BoB, (c) magnitude of monthly average of wind speed perpendicular to coast (WPC) (m s^{-1}) derived from CCMP averaged over the box 10.0°N–15.0°N and 80.0°E–82.0°E (marked as a blue box in inset map; zonal wind speed) in the southwestern BoB (blue line) and averaged over the box 19.5°N–21.5°N; 87.0°E–90.5°E (marked as a green box in inset map; meridional wind speed) in the northern BoB (green line) (d) blue line: monthly average of the minimum temperature difference ($\Delta T_{L\text{-}O_MN}$) between land (T_L; 10.0°N–15.0°N and 78.0°E–80.0°E; marked as a blue box over land in inset map) and ocean (T_O; 10.0°N–15.0°N and 80.0°E–82.0°E; marked as a blue box over the ocean in inset map) during the night derived from ERA5 air temperature (°C) and green line: monthly average of the minimum temperature difference between land (T_L; 21.5°N–23.5°N; 87.0°E–90.5°E; marked as a green box over land in inset map) and ocean (T_O; 19.5°N −21.5°N; 87.0°E–90.5°E; marked as a green box over the ocean in inset map) during the night derived from ERA5 air temperature (°C) and (e) a non-dimensional land breeze index (WPC^2/$C_p|\Delta T_{L\text{-}O\_MN}|$) in the southwestern BoB (blue line) and northern BoB (green line). In panel (e), the black line represents an ILBS of magnitude −3, below which the offshore temperature gradient is insufficient to overcome the opposing wind toward land, which restricts the Land Breeze System to the coastal region. WS = $\sqrt{U^2 + V^2}$ based on the highest temporal resolution data and $\overline{W}$ is vector wind.

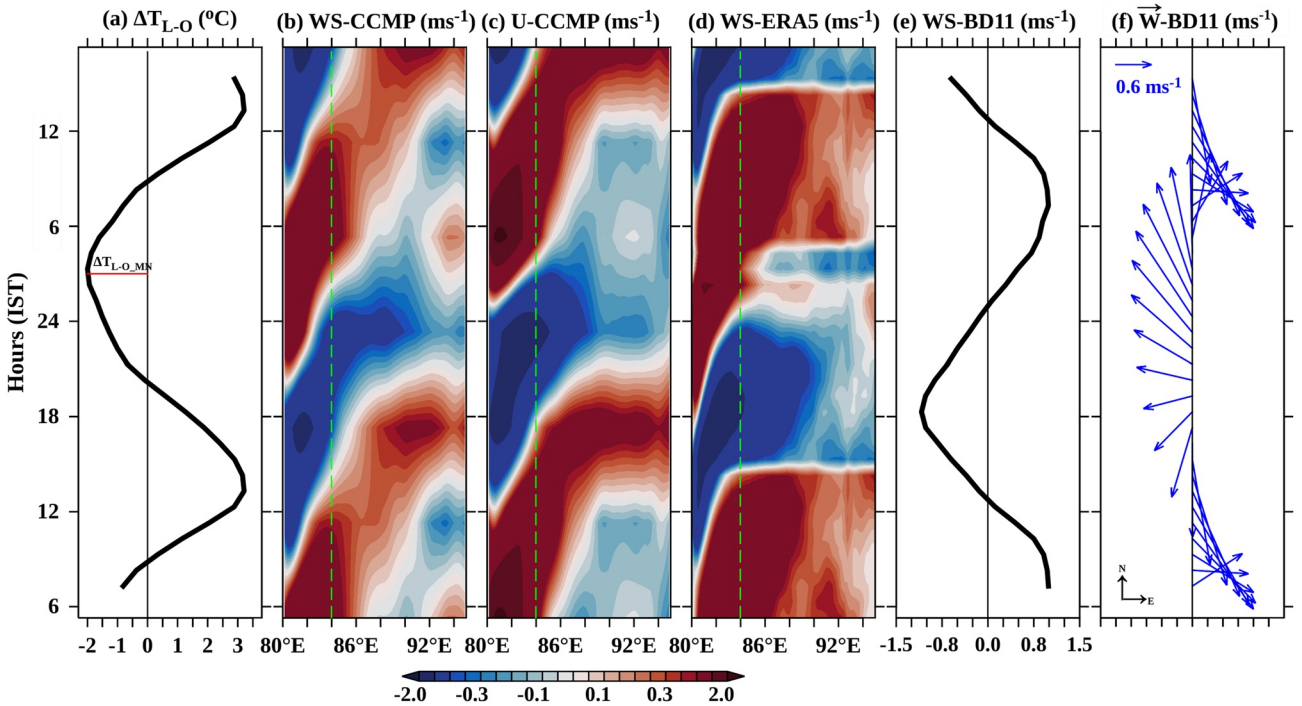

Figure 6. The composite of (a) sub-daily evolution of air-temperature difference ($\Delta T_{L\text{-}O}$; °C) between land (T_L; 10.0°N–15.0°N and 78.0°E–80.0°E) and ocean (T_O; 10.0°N–15.0°N and 80.0°E–82.0°E) during July–August derived from ERA5. The minimum value of the air-temperature difference between land (T_L) and ocean (T_O) observed during the night is marked as $\Delta T_{L\text{-}O\_MN}$. Sub-daily evolution of (b) Cross-Calibrated Multi-Platform (CCMP) wind speed anomaly (WS; m s^{-1}), (c) CCMP zonal wind speed anomaly (U; m s^{-1}), (d) ERA5 wind speed anomaly (WS; m s^{-1}) during July–August averaged over latitude band 10.0°N–15.0°N. Sub-daily evolution (e) magnitude of wind speed anomaly (WS; m s^{-1}) and (f) wind vector anomaly ($\overrightarrow{W}$; m s^{-1}) derived from the BD11 mooring during July–August. For better readability, the *y*-axis is repeated for half-day. The longitude (84.0°E) corresponding to the mooring location is marked as green dashed vertical lines in panels (b)–(d). A three-point running mean is applied to BD11 and ERA5 data for better readability. WS = $\sqrt{U^2 + V^2}$ based on the highest temporal resolution data and $\overrightarrow{W}$ is vector wind.Time in IST hours.

February, followed by a sharp decrease in negative values, reaching a minimum negative value around May (−2°C) (Figure 5d; blue line). Subsequently, the magnitude of the negative differences progressively increases between May and November (Figure 5d; blue line). Larger negative values of $\Delta T_{L\text{-}O\_MN}$ from November to February provide favorable conditions for the LBS in the southwestern BoB. However, the maximum negative values $\Delta T_{L\text{-}O\_MN}$ coincide with the period when the LBS shows minimum offshore extension in the southwestern BoB (Figure 4a; blue box and Figure 5d; blue line). The magnitude of $\Delta T_{L\text{-}O\_MN}$ during July and August, when the LBS displays maximum offshore extension, ranges from −0.8°C to −0.1°C, which is much smaller than its magnitude between November and February (Figure 5d; blue line). These characteristics suggest that the annual distribution of $\Delta T_{L\text{-}O\_MN}$ alone cannot explain seasonal variations in the offshore extension of the LBS in the southwestern BoB.

The prevailing wind in the southwestern BoB is southwesterly (offshore) from June to September and northeasterly (onshore) between November to February, with a magnitude of 10 m s^{-1} in the summer and 8 m s^{-1} in the late fall and early winter (Figure 5a). The wind speed magnitude is much smaller (~6 m s^{-1}) and predominately easterly (onshore) in March, April, and October; and weak southerly (parallel to the coast) in May (Figure 5a). The zonal wind in the southwestern BoB is onshore with a magnitude of −2 to −4 m s^{-1} between October and March, such that it opposes the LBS (Figure 5c; blue line). On the other hand, the prevailing zonal wind direction is offshore, and its magnitude reaches 6 m s^{-1} between May and September, a condition favorable for the offshore extension of LBS in the southwestern BoB (Figure 5c; blue line).

We use a dimensionless LBS index (ILBS) proposed by Biggs and Graves (1962), expressed as

$$\mathrm{ILBS} = \begin{cases} -\dfrac{\mathrm{WPC}^2}{C_{p|\Delta T_{\mathrm{L-O\_MN}}|}}, \mathrm{WPC} < 0\,(\mathrm{onshore}) \\ \dfrac{\mathrm{WPC}^2}{C_{p|\Delta T_{\mathrm{L-O\_MN}}|}}, \mathrm{WPC} \geq 0\,(\mathrm{offshore}) \end{cases} \quad (1)$$

to understand the competing effects of $\Delta T_{\mathrm{L\text{-}O\_MN}}$ and opposing winds on the LBS in the southern BoB. In this expression Equation 1, C_p is the specific heat capacity of air (1.003 kJ K^{-1} kg^{-1}), *WPC* is a component of wind perpendicular to the coast (zonal wind speed in the southwestern BoB), and $|\Delta T_{\mathrm{L\text{-}O\_MN}}|$ is the magnitude of the minimum value in the difference between T_L and T_O. The ILBS will be negative when the WPC is onshore (i.e., westward in the southwestern BoB) and positive when WPC is offshore (i.e., eastward in the southwestern BoB). Values of ILBS less than −3 are indicative of a $\Delta T_{\mathrm{L\text{-}O\_MN}}$ that is insufficient to overcome the opposing zonal wind speed (Biggs & Graves, 1962; Porson et al., 2007).

Consistent with this threshold, the LBS is largely absent in the southwestern BoB between November and February when the ILBS magnitude is below −3 (Figure 5e; blue line). From March onwards, values of ILBS are higher than −3, and LBS starts to emerge in the offshore region of southwestern BoB (Figure 4a). Between June and August, ILBS became strongly positive, coinciding with the maximum offshore extension of LBS (Figure 5e; blue line). These characteristics suggest that the prevailing zonal winds in the southwestern BoB is a dominant factor in determining the annual variability in strength and geographical coverage of LBS in the southwestern BoB.

The seasonality of the LBS signature in the northern BoB can also be explained by the annual variability of ILBS (Figure 5e; green line). The LBS is largely absent in the northern BoB between April and September when the ILBS magnitude is below −3, which is primarily attributed to prevailing onshore (i.e., northward) winds with speeds of 5–6 m s^{-1} (Figure 4a; green line in Figures 5c and 5e). On the other hand, due to the offshore (i.e., southward) prevailing wind with speeds of 4 m s^{-1} between October and March, ILBS are greater than −3 in the northern BoB, and LBS signature is noticeable in the offshore region (Figures 4a and 5b; green line in Figures 5c and 5e). The presence of strong alongshore wind speed during much of the year is consistent with the absence of an extensive offshore LBS in the northwestern BoB coast (between 16.0°N and 20.0°N) in most of the months (Figure 4a and Figure S1 in Supporting Information S1).

The above analysis indicates that the amplitude of LBS signature in the northern and northwestern BoB regions is relatively small and occupies only a small region. On the other hand, the LBS signature in the southwestern BoB is much stronger and shows substantial spatial coverage. Hence, in the analysis that follows, we restrict ourselves to July and August in the southwestern BoB, when the LBS shows maximum strength and geographical coverage. It is also during this time that the mooring BD11 comes under the influence of diurnal variability of wind speed in the southwestern BoB (Figure 4a; blue box).

3.3. Spatio-Temporal Evolution of LBS in the Southwestern BoB During July–August

The coast is meridionally oriented in the southwestern BoB, and the offshore flow associated with LBS is dominated by a zonal component of wind speed. Hence, we restrict our analysis to primarily total wind speed and its zonal component. The Hovmöller diagram of diurnal wind speed anomaly and zonal wind speed anomaly averaged over a latitude band between 10.0°N and 15.0°N during July–August shows an alternative band of positive and negative values with apparent eastward propagation (Figures 6b and 6c). These particular characteristics of the eastward propagating signal in the composite field of zonal wind speed anomaly are evident in week-long continuous time series observations in the southwestern BoB during 22–29 July 2017 (Figure 3a).

The sub-daily evolution of the Hovmöller diagram of zonal wind speed anomaly shows the initiation of eastward wind speed anomaly around 2000 IST along the coastal region of the southwestern BoB as soon as air temperature values over the land are cooler than the nearby ocean (Figures 6a and 6c). The magnitude of the eastward wind anomaly intensifies further and propagates eastward between 0100 and 1300 IST (Figure 6c). The zonal wind anomaly becomes westward in the coastal region of the southwestern BoB around 1300 IST, and this anomaly propagates eastward when air temperature values over the land are warmer than the nearby ocean (Figures 6a and 6c).

The prevailing large-scale wind in the southwestern BoB during July–August is southwesterly (Figure S1 in Supporting Information S1). Hence, the eastward-blowing LBS can lead to an increase in the total wind speed. Similarly, the westward blowing sea breeze signal can cause a decrease in the total wind speed. The

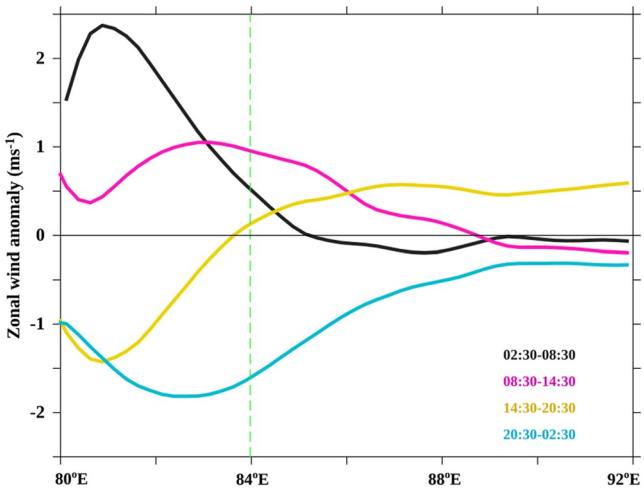

Figure 7. The composite of longitudinal distribution of Cross-Calibrated Multi-Platform zonal wind anomaly (m s^{-1}) averaged over the latitude band 10.0°N–15.0°N in the southwestern Bay of Bengal during July–August during four different times in a day (black: 02:30–08:30 IST; pink: 08:30–14:30 IST; yellow: 14:30–20:30 IST and light blue: 20:30–02:30 IST). Positive and negative values represent offshore/eastward and onshore/westward zonal wind speed anomalies, respectively. The green dashed vertical line represents BD11 mooring at 13.5°N, 84.0°E.

modulation of background large-scale wind speed can be inferred from the Hovmöller diagram of wind speed anomaly, in which the magnitude of wind speed increases (~2 m s^{-1}) when the LBS persists in the southwestern BoB (Figure 6b).

We note that the timing of onset and subsequent propagation of wind speed and zonal wind speed anomalies observed on the southwestern BoB are roughly in agreement with previous studies that examined the LBS in other parts of the globe (Davis et al., 2019; Rafiq et al., 2020; Short et al., 2019). For instance, using multi-satellite scatterometer observation in the eastern equatorial Indian Ocean, Short et al. (2019) reported the existence of LBS between 0000 and 1300 LST. These characteristics further corroborate our argument that the diurnal variability of wind speed on the southwestern BoB is the signature of the LBS.

The signature of the eastward propagating zonal wind speed anomaly is apparent out to 87.0°E (~700 km offshore) in the southwestern BoB (Figures 6c and 7). Further to the east of 87.0°E, the eastward propagating zonal wind speed anomaly tapers to zero (Figures 6c and 7). Compared to the coastal zone, the amplitude of zonal wind speed anomaly is reduced by half at the 84.0°E BD11 mooring location (Figure 7). The faster propagating characteristics of the LBS signal in the region far offshore are consistent with diurnal wind perturbation studies around the Maritime Continent of the eastern equatorial Indian Ocean (Figure 5 of Short et al., 2019). Short et al. (2019) conjecture that this offshore feature is independent of the LBS signal. Instead, they attribute this feature to the downward penetration of momentum due to the growth of planetary boundary layer instabilities associated with daytime warming of the near-surface layer (Dai & Deser, 1999).

The signature of LBS is apparent in the wind speed measurements from BD11 mooring, located approximately 400 km from the southwest coast of India (Figures 3a, 6e, and 6f). A time series of the wind speed anomaly derived from BD11 mooring shows a well-defined diurnal variability with an enhancement between 0000–1200 and a reduction between 1200–0000 IST in conjunction with the arrival of the eastward propagating zonal wind speed anomaly at the mooring location (Figures 3a and 3c; Figures 6c and 6e). The signature of the LBS is conspicuous in the July–August composite of the sub-daily evolution of wind vector derived from the BD11 (Figure 6f). The well-defined clockwise rotation of wind vector anomaly at the mooring location is consistent with the behavior of the LBS in the northern hemisphere (Figure 6f) (Gille et al., 2005). An eastward wind anomaly, the signature of LBS, is apparent at the BD11 by 0600 IST, intensifies, and then vanishes by 1600 IST (Figure 6f). Subsequently, a westward wind anomaly is evident at the mooring between 2000 and 0600 IST (Figure 6f). The frequency distribution of the diurnal range of wind speed anomaly during July and August shows that the magnitude is higher than 2 m s^{-1} in approximately 58% of days with an average value of around 1.7 ± 0.02 m s^{-1} (Figure 8a and Figure S2 in Supporting Information S1).

The approximate time lag between the reversal of zonal wind anomaly in the coastal region and at the BD11 mooring is around 6 hr, indicating that the phase speed of these eastward propagating features is around 15 m s^{-1}. This estimated phase speed is comparable to previous estimates of offshore propagation (~11–30 m s^{-1}) associated with the LBS due to gravity waves (Davis et al., 2019; Kilpatrick et al., 2017).

3.4. Impact of the LBS on Oceanographic and Atmospheric Parameters

We might expect the remarkable diurnal variability in wind speed associated with the LBS to play a role in modulating oceanographic and other atmospheric parameters in the open ocean region of southwestern BoB. We next examine the effect of LBS wind speeds on ocean surface currents and LHF using the buoy data, HF radar, and the ERA5 reanalysis focusing on the months of July and August.

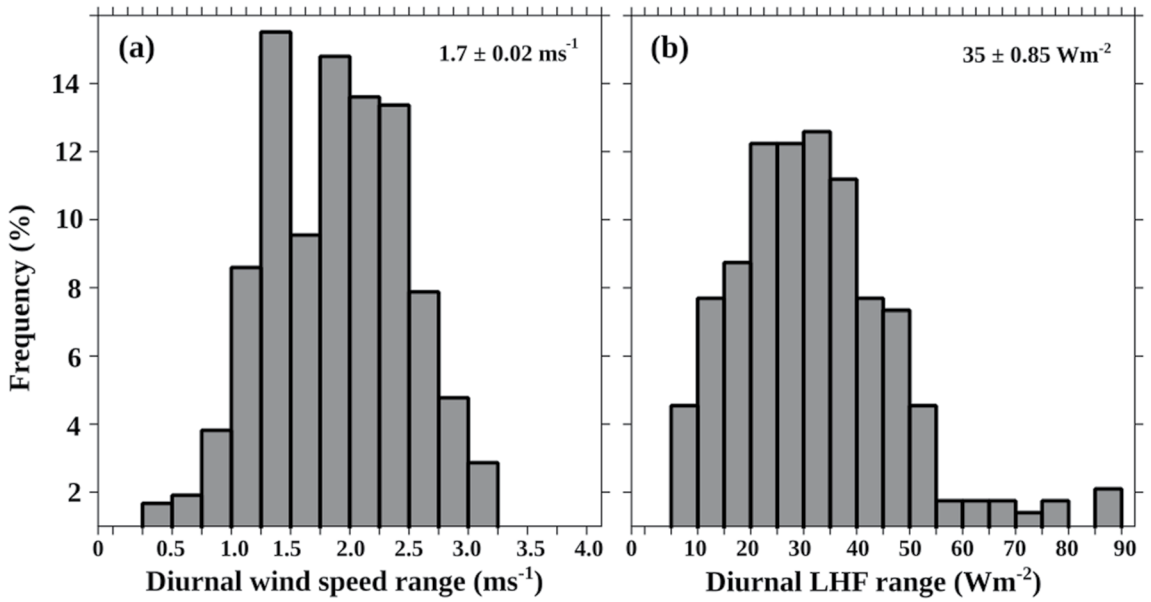

Figure 8. The frequency of the diurnal range in (a) wind speed (m s^{-1}) in 0.25 m s^{-1} bins and (b) latent heat flux (LHF) (W m^{-2}) in 5 W m^{-2} bins during July and August. The wind speed and LHF data are bandpass filtered between periods of 22.5–25.5 hr before estimating the diurnal range of individual days (as illustrated in Figure S2 in Supporting Information S1).

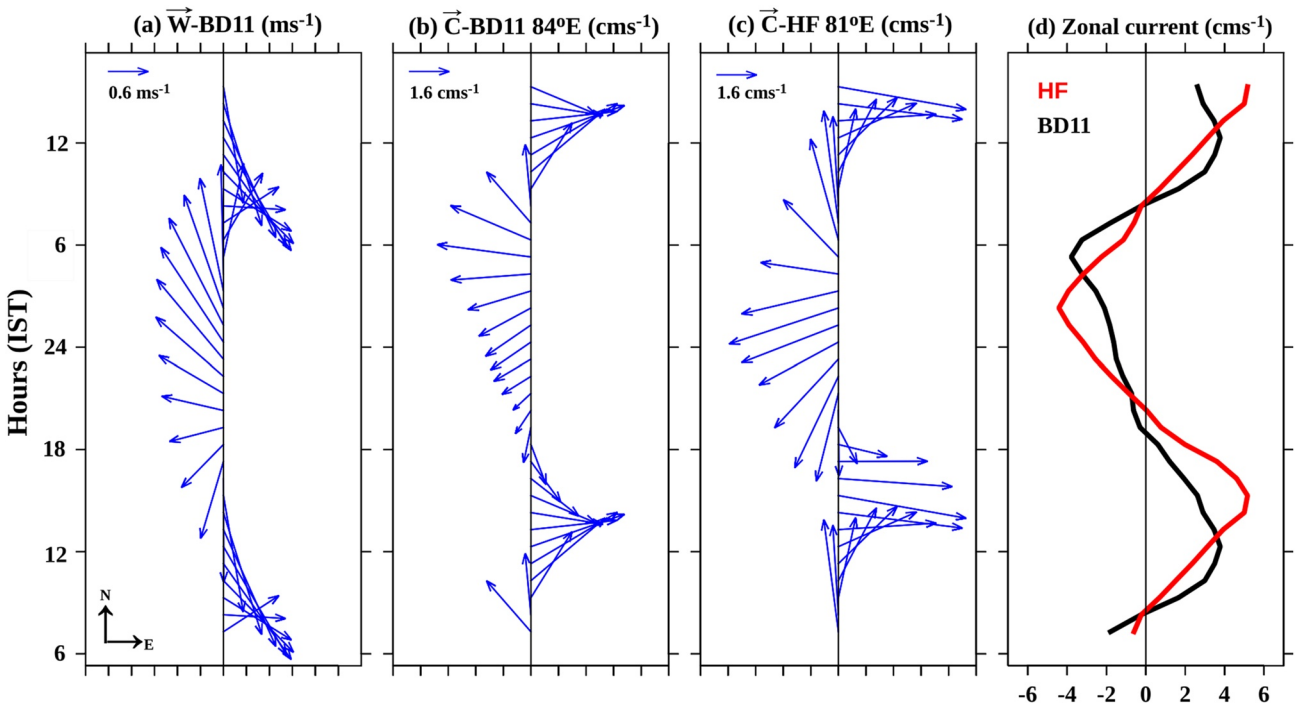

Figure 9. The composite of sub-daily evolution (a) BD11 wind vector anomaly ($\overrightarrow{W}$; m s^{-1}), current vector anomaly ($\overrightarrow{C}$; cm s^{-1}) derived from (b) BD11 mooring at 13.5°N, 84.0°E and (c) high frequency (HF) radar at 81.0°E averaged over 11.0°E–12.0°N and (d) magnitude of zonal current speed anomaly (cm s^{-1}) from HF radar (red) and BD11 (black). For better readability, the *y*-axis is repeated for half-day, and a three-point running mean is applied to BD11 and HF radar data. $\overrightarrow{W}$ is vector wind and $\overrightarrow{C}$ is vector current. Time in IST hours.

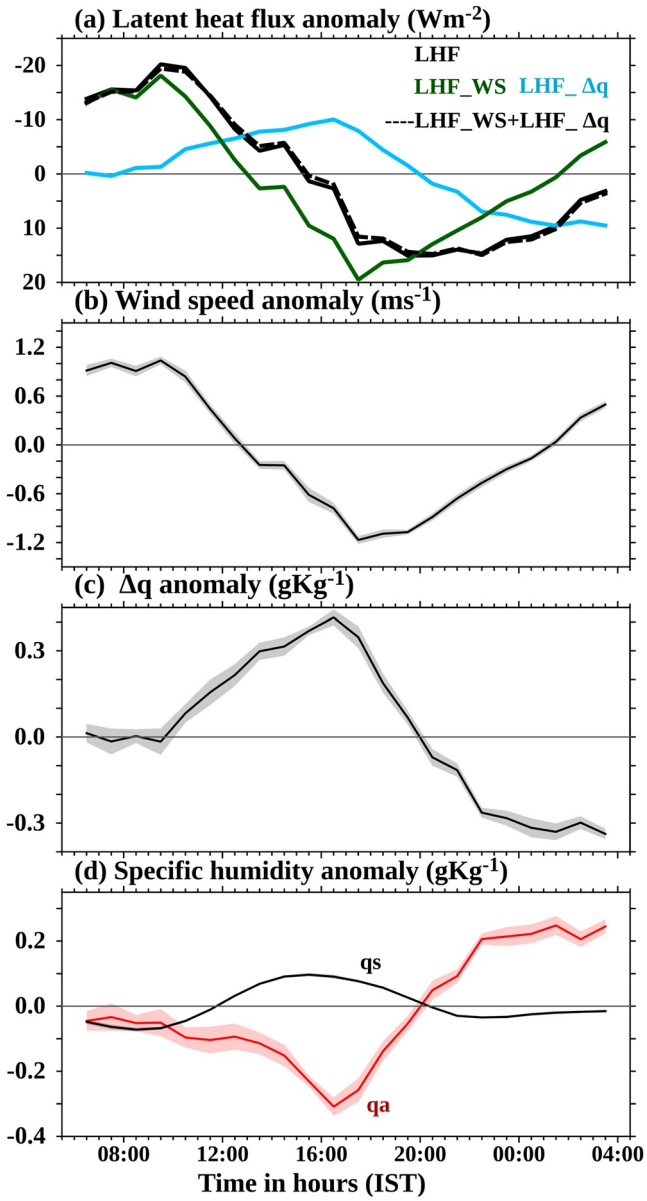

Figure 10. Composite evolution of sub-daily variability of the anomaly of (a) latent heat flux (LHF) (black; W m^{-2}) (b) wind speed (m s^{-1}), (c) specific humidity difference between air and sea (Δq; $q_s - q_a$; g kg^{-1}), (d) specific humidity of air (q_a) (red) and specific humidity at the sea surface (q_s) (black) derived from BD11 mooring during July and August. Panel (a) shows LHF derived from BD11 mooring data after retaining only sub-daily variability in wind speed (LHF_WS; green line), only sub-daily variability in air-sea specific humidity differences (LHF_Δq; blue line), and the sum of LHF_WS and LHF_Δq (black dashed line). The shading represents the one standard error mean estimated based on the standard deviation of data in each hourly bin.

3.4.1. Impact on Surface Currents

The impact of diurnal wind speed variability associated with the LBS on the ocean surface currents in the southwestern BoB is illustrated in Figures 9a–9d. The near-surface current vector anomalies derived from the buoy and HF radar data are very similar, and like the wind vector anomalies show clockwise rotation. Eastward currents are strongest between 1000 and 1800 IST with a maximum of ∼6 cm s^{-1} around 1200 IST, and westward currents are strongest between 1800 and 0800 IST with a maximum magnitude of ∼−6 cm s^{-1} around 0100 IST (Figures 9c and 9d; red line). The seasonal average of current speed at the BD11 buoy during summer is ∼27 cm s^{-1}. Hence, the ∼12 cm s^{-1} diurnal range of the current speed anomaly at the BD11 buoy is approximately 45% of the total current magnitude during July and August (Figure 9d; black line).

The direction of the current vector anomaly is approximately 90° left to the wind direction (Figures 9a–9c). Previous studies on the LBS, particularly on the north of 30°N, where the inertial period is less than a day, showed that the current modulation with respect to diurnal wind forcing is as expected from classical Ekman drift theory (Fontán et al., 2013; Rafiq et al., 2020) in which the current is directed to the right of the winds. In our case, the inertial period is ∼2 days at the buoy location, which is much longer than the diurnal time scale of the LBS wind forcing. Thus, the land and sea-breeze forced currents are superinertial in frequency, for which the currents are theoretically expected to spiral to the left of clockwise rotating winds (Orlic, 2011; Rudnick and Weller, 1993).

3.4.2. Impact on LHF

The sub-daily variability of the LHF anomaly at the BD11 mooring location shows a well-defined diurnal variability with a peak heat loss at 1000 IST and a minimum heat loss from the ocean around 2000 IST (Figure 10a; black line). Wind speed and air-sea specific humidity difference (Δq) are the two main factors that determine the modulation of LHF. Our analysis at the BD11 buoy location shows that the bulk of the diurnal modulation in LHF is determined by the diurnal variability of wind speed associated with the LBS. There is a strong temporal correspondence between wind speed and LHF with an enhancement and reduction in LHF loss from the ocean in conjunction with a maximum and minimum in wind speed (Figures 10a and 10b). The contribution of Δq to the modulation of diurnal variability of LHF is relatively small, and is in opposition to the impact of diurnal wind speed variability on LHF (Figures 10a and 10c).

The enhancement of Δq during the afternoon (∼0.4 g kg^{-1}) is due to the combined effect of reduction in air-specific humidity (q_a) and increasing specific humidity at the sea surface (q_s) (Figure 10d). Generally, the sub-daily variability of q_s follows SST, reaching maximum in the afternoon (Figure S3 in Supporting Information S1). However, q_a declines during the afternoon when both SST and q_s show an enhancement (Figure 10d). One plausible explanation for the reduction in q_a is the entrainment of the dry planetary boundary layer air into the surface layer due to atmospheric mixed layer growth, as demonstrated in previous studies (Johnson & Ciesielski, 2017). These characteristics indicate that the diurnal variability of wind speed associated with LBS is primarily responsible for the diurnal variability of LHF in the southwestern BoB during July and August.

The frequency distribution of the diurnal range in LHF during July and August shows that its magnitude is higher than 25 W m^{-2} approximately 68% of the time, with an average value of around 35 ± 0.85 W m^{-2} (Figures 8b and 10a; black line). Occasionally, the diurnal range of LHF may be as large as 75 W m^{-2} (Figure 11d; blue line and Figure 8b). The mean value of LHF during July and August at the mooring location is around 110 W m^{-2}, so

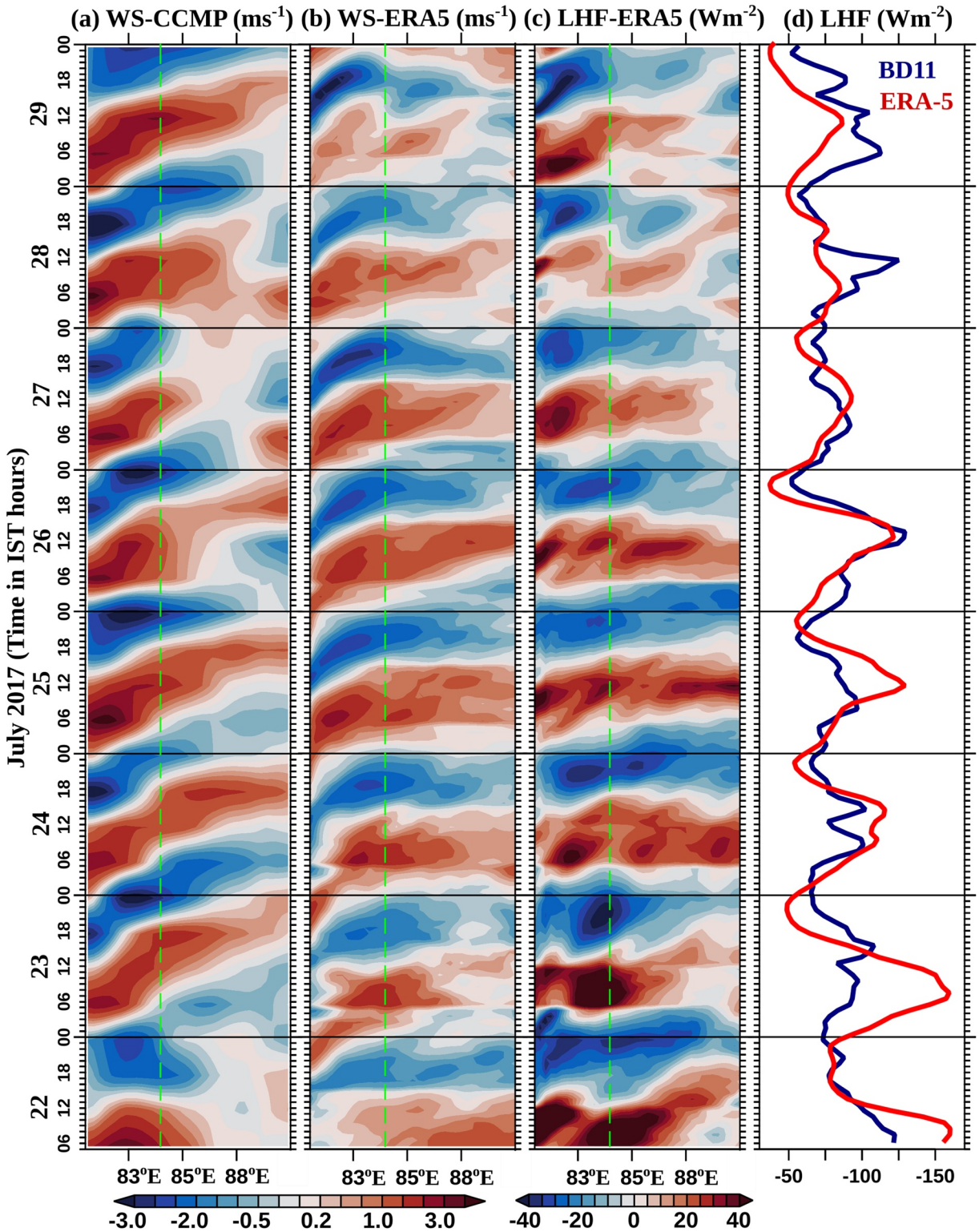

Figure 11. Temporal evolution of longitudinal evolution of (a) Cross-Calibrated Multi-Platform 6-hourly wind speed anomaly (WS; m s^{-1}), (b) ERA5 hourly wind speed anomaly (WS; m s^{-1}), (c) ERA5 hourly latent heat flux (LHF) anomaly (W m^{-2}), and (d) LHF anomaly (W m^{-2}) derived from BD11 (blue) and ERA5 (red) at the exact location of the buoy (13.5°N, 84.0°E) in the southwestern Bay of Bengal during 22–29 July 2017. A three-point running average is applied to ERA5 and BD11 parameters for better readability. The longitude (84.0°E) corresponding to the BD11 location is marked as green dashed vertical lines in panels (a)–(c). WS = $\sqrt{U^2 + V^2}$ based on the highest temporal resolution data. Time in IST hours.

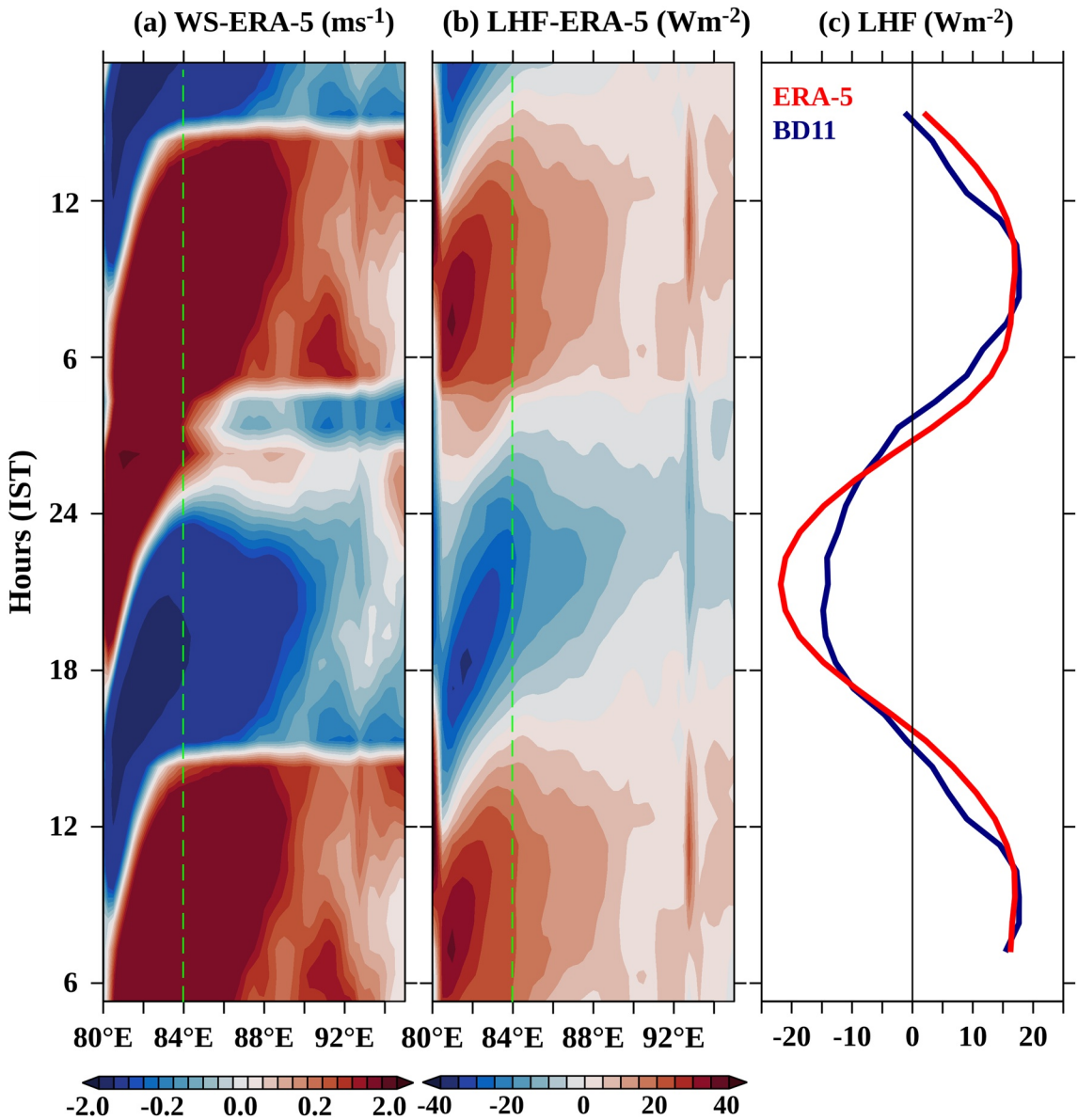

Figure 12. The composite of sub-daily evolution (a) wind speed anomaly (WS; m s^{-1}), (b) latent heat flux (LHF) anomaly (W m^{-2}) from ERA5, and (c) LHF anomaly (W m^{-2}) from BD11 (blue) and ERA5 (red) at mooring location (13.5°N, 84.0°E) during July and August. The longitude (84.0°E) corresponding to the BD11 location is marked as green dashed vertical lines in panels (a) and (b). For better readability, the *y*-axis is repeated for half-day, and a three-point running mean is applied to BD11 and ERA5 data for better readability. WS = $\sqrt{U^2 + V^2}$ based on the highest temporal resolution data. Time in IST hours.

that the ~35 W m^{-2} diurnal range associated with LBS is approximately 30% of the magnitude of the seasonal mean value of LHF in the southwestern BoB.

We used the ERA5 reanalysis to examine the spatial coherence of LHF variability observed at the mooring location associated with wind speed due to the LBS (Figures 11c and 11d; red line, Figures 12b and 12c; red line). Diurnal variability of LHF from ERA5 shows an excellent agreement with BD11 observations, both in phase and amplitude (Figures 11d and 12c). In addition, the diurnal modulation of LHF by wind speed is well represented in ERA5 as in the BD11 observation (Figures 6b, 6d, 11a, 11b, and 11d). Also, the eastward propagating wind speed anomaly and zonal wind speed anomaly observed in the CCMP wind product are well captured in ERA5 (Figures 11a and 11b; Figures 3a and 3b). These characteristics suggest that the LBS in the southwestern BoB is well represented in the ERA5, and it provides an opportunity to examine the spatial coherence of diurnal variability of LHF observed at the BD11 mooring location.

Consistent with the eastward propagation of enhancement and reduction in the wind speed anomaly associated with the LBS, the LHF loss from the ocean derived from the ERA5 in the southwestern BoB shows a well-defined diurnal variability (Figures 12a and 12c; red line). The average magnitude of the diurnal range in LHF (35 W m^{-2}) estimated from ERA5 agrees well with that from BD11 (Figure 12c). However, the higher magnitude diurnal wind speed range (4 m s^{-1}) west of the BD11 mooring location means an even greater diurnal range for LHF derived from ERA5 there (Figures 12a and 12b). Thus, the LBS has a significant impact on sub-daily LHF variability in the offshore regions of the southwestern BoB.

4. Summary and Conclusion

In this study, we examined the seasonal variability of the LBS in the southwestern BoB and its impact on the near-surface current field and LHF. For this purpose, we used moored buoy measurements with 1-hr temporal resolution at 13.5°N, 84.0°E, coastal radar data, an atmospheric reanalysis, and CCMP wind velocity data. We found a seasonal variation of the LBS in the southwestern BoB with a maximum diurnal wind speed amplitude (~2 m s^{-1}) and geographical coverage during the Southwest Monsoon in July and August and a minimum during the Northeast Monsoon in December and January. During the peak phase, the signature of the LBS in the southwestern BoB occupies approximately 20% of the BoB basin and accounts for about 15% of the total wind speed variance during July–August. Annual variability in LBS is also observed in the northern BoB, though roughly opposite in temporal evolution from that in the southwestern BoB, with a maximum diurnal wind speed amplitude during November-February and a minimum during June and August. It is also found that the LBS signal in the northern BoB shows much smaller geographical coverage during its peak phase compared to the southwestern BoB.

Consistent with previous work, the present study indicates that the LBS occurs predominantly due to the differential heating between the ocean and land in the southwestern BoB. Our analysis further suggests that the prevailing zonal winds are a dominant factor in determining the annual variability in strength and geographical coverage of the LBS in the southwestern BoB. In particular, westward (onshore) winds from November to February restrict the offshore extension of LBS, though higher negative values of $\Delta T_{\text{L-O\_MN}}$ (the minimum value of the difference between temperature over land and temperature over the ocean during the night) provide favorable conditions for LBS development. In contrast, $\Delta T_{\text{L-O\_MN}}$ magnitude from May to October is smaller than for November to February, but eastward prevailing winds provide favorable conditions for maximum geographical coverage of the LBS. The seasonality of the LBS in the northern BoB is also determined by the prevailing winds, such that the LBS is largely absent in the northern BoB between April and September due to prevailing onshore (northward) winds. In contrast, due to the offshore (southward) prevailing winds between October and March, the LBS signature is evident in the offshore region of the northern BoB.

Air-sea interaction processes associated with LBS in the southwestern BoB during July–August, when the LBS shows maximum geographical coverage and strength, are examined using in-situ data from the mooring and HF radar. The near-surface current vector anomaly derived from the mooring and HF radar data shows a rapid response to the diurnally evolving wind vector anomaly. Eastward currents are observed between 1000 and 1800 IST with a maximum magnitude (~6 cm s^{-1}) around 1200 IST, and westward currents are observed between 1800–0800 IST with a maximum magnitude (~−6 cm s^{-1}) around 0100 IST. The currents were to the left of the clockwise rotating surface winds, consistent with the theory for superinertial flows. We also found a well-defined diurnal variability in latent heat loss from the ocean in conjunction with diurnally evolving wind speed due to the LBS in the southwestern BoB. The magnitude of the diurnal range of LHF due to LBS is typically around 35 W m^{-2}, but can at times be as large as 75 W m^{-2}.

The present study indicates that failure to represent the LBS in the southwestern BoB may result in an inaccurate representation of LHF and consequently in the simulation of SST. In particular, the inability of coupled models to represent the LBS in the BoB may lead to accumulated errors in net surface heat flux that potentially impact the accuracy of subseasonal, seasonal and interannual time scale simulations. A detailed observational analysis of the LBS on SST in the BoB will be the subject of a separate study. Likewise, we have undertaken a more detailed dynamical analysis of the observed superinertial flow in relation to LBS wind forcing.

Data Availability Statement

CCMP Version-2.0 vector wind analyses are produced by Remote Sensing Systems. Data are available at www.remss.com. The ERA5 data set was obtained from the Copernicus Climate Change Service Climate Data Store (CDS) website (at https://cds.climate.copernicus.eu/cdsapp%23%21/home), accessed on 1 June 2022. OMNI mooring data is available at https://incois.gov.in/portal/datainfo/buoys.jsp. The HF radar data used in this study is accessible at http://odis.incois.gov.in/index.php/insitu-data/coastal-hf-radar/data. The Matlab code for coare3.6 is obtained from http://ftp1.esrl.noaa.gov/BLO/Air-Sea/bulkalg/cor3_6/.

Acknowledgments
The encouragement and facilities provided by the Director, INCOIS, are gratefully acknowledged. The authors thank two anonymous reviewers for their extensive and constructive comments and suggestions which greatly helped to improve the manuscript. OMNI moorings and HF radar network are maintained by NIOT, Chennai. Graphics were generated using PyFerret. Athulya acknowledges the support provided by the Council of Scientific & Industrial Research (CSIR) Research Fellowships as part of the Ph.D. program. This is INCOIS contribution number 483 and PMEL contribution number 5439.

References

Aparna, A. R., & Girishkumar, M. S. (2022). Mixed layer heat budget in the eastern equatorial Indian Ocean during the two consecutive positive Indian Ocean dipole events in 2018 and 2019. *Climate Dynamics*, *58*(11–12), 3297–3315. https://doi.org/10.1007/S00382-021-06099-8

Aparna, M., Shetye, S. R., Shankar, D., Shenoi, S. S. C., Mehra, P., & Desai, R. G. P. (2005). Estimating the seaward extent of sea breeze from QuikSCAT scatterometry. *Geophysical Research Letters*, *32*(13), 1–4. https://doi.org/10.1029/2005GL023107

Bernie, D. J., Woolnough, S. J., Slingo, J. M., & Guilyardi, E. (2005). Modeling diurnal and intraseasonal variability of the ocean mixed layer. *Journal of Climate*, *18*(8), 1190–1202. https://doi.org/10.1175/JCLI3319.1

Bhat, G. S., & Fernando, H. J. S. (2016). Remotely driven anomalous sea-air heat flux over the north Indian Ocean during the summer monsoon season. *Oceanography*, *29*(2), 232–241. https://doi.org/10.5670/oceanog.2016.55

Bhat, G. S., Gadgil, S., Hareesh Kumar, P. V., Kalsi, S. R., Madhusoodanan, P., Murty, V. S. N., et al. (2001). BOBMEX: The Bay of Bengal monsoon experiment. *BAMS*, *82*(10), 2217–2244. https://doi.org/10.1175/1520-0477(2001)082

Biggs, W. G., & Graves, M. E. (1962). A lake breeze index. *Journal of Applied Meteorology*, *1*(4), 474–480. https://doi.org/10.1175/1520-0450(1962)001<0474:albi>2.0.co;2

Chen, X., Zhang, F., & Zhao, K. (2016). Diurnal variations of the land-sea breeze and its related precipitation over South China. *Journal of the Atmospheric Sciences*, *73*(12), 4793–4815. https://doi.org/10.1175/JAS-D-16-0106.1

Clancy, R. M., Thompson, J. D., Hurlburt, H. E., & Lee, J. D. (1979). A model of mesoscale air-sea interaction in a sea breeze-coastal upwelling regime. *Monthly Weather Review*, *107*(11), 1476–1505. https://doi.org/10.1175/1520-0493(1979)107<1476:amomas>2.0.co;2

Cyriac, A., Ghoshal, T., Shaileshbhai, P. R., & Chakraborty, A. (2016). Variability of sensible heat flux over the Bay of Bengal and its connection to Indian Ocean Dipole events. *Ocean Science Journal*, *51*(1), 97–107. https://doi.org/10.1007/S12601-016-0009-9

Dai, A., & Deser, C. (1999). Diurnal and semidiurnal variations in global surface wind and divergence fields. *Journal of Geophysical Research*, *104*(D24), 31109–31125. https://doi.org/10.1029/1999JD900927

Davis, S. R., Farrar, J. T., Weller, R. A., Jiang, H., & Pratt, L. J. (2019). The land-sea breeze of the red sea: Observations, simulations, and relationships to regional moisture transport. *Journal of Geophysical Research: Atmospheres*, *124*(24), 13803–13825. https://doi.org/10.1029/2019JD031007

Dey, D., Sil, S., Jana, S., Pramanik, S., & Pandey, P. C. (2017). An assessment of TropFlux and NCEP air-sea fluxes on ROMS simulations over the Bay of Bengal region. *Dynamics of Atmospheres and Oceans*, *80*, 47–61. https://doi.org/10.1016/J.DYNATMOCE.2017.09.002

Duncan, B., & Han, W. (2009). Indian Ocean intraseasonal sea surface temperature variability during boreal summer: Madden-Julian Oscillation versus submonthly forcing and processes. *Journal of Geophysical Research*, *114*(C5), 5002. https://doi.org/10.1029/2008JC004958

Edson, J. B., Jampana, V., Weller, R. A., Bigorre, S. P., Plueddemann, A. J., Fairall, C. W., et al. (2013). On the exchange of momentum over the open ocean. *Journal of Physical Oceanography*, *43*(8), 1589–1610. https://doi.org/10.1175/JPO-D-12-0173.1

Fairall, C. W., Bradley, E. F., Hare, J. E., Grachev, A. A., & Edson, J. B. (2003). Bulk parameterization of air-sea fluxes: Updates and verification for the COARE algorithm [Software]. Journal of Climate, *16*(4), 571–591. https://doi.org/10.1175/1520-0442(2003)016<0571:BPOASF>2.0.CO;2

Fairall, C. W., Bradley, E. F., Rogers, D. P., Edson, J. B., & Young, G. S. (1996). Bulk parameterization of air-sea fluxes for tropical ocean global atmosphere coupled-ocean atmosphere response experiment. *Journal of Geophysical Research*, *101*(C2), 3747–3764. https://doi.org/10.1029/95JC03205

Fontán, A., Esnaola, G., Sáenz, J., & González, M. (2013). Variability in the air–sea interaction patterns and timescales within the southeastern Bay of Biscay, as observed by HF radar data. *Ocean Science*, *9*(2), 399–410. https://doi.org/10.5194/os-9-399-2013

Giglio, D., Gille, S. T., Cornuelle, B. D., Subramanian, A. C., Turk, F. J., Hristova-Veleva, S., & Northcott, D. (2022). Annual modulation of diurnal winds in the tropical oceans. *Remote Sensing*, *14*(3), 459. https://doi.org/10.3390/rs14030459

Gille, S. T., Llewellyn Smith, S. G., & Lee, S. M. (2003). Measuring the sea breeze from QuikSCAT scatterometry. *Geophysical Research Letters*, *30*(3), 3–6. https://doi.org/10.1029/2002GL016230

Gille, S. T., Llewellyn Smith, S. G., & Statom, N. M. (2005). Global observations of the land breeze. *Geophysical Research Letters*, *32*(5), 1–4. https://doi.org/10.1029/2004GL022139

Girishkumar, M. S., Joseph, J., McPhaden, M. J., & Pattabhi Ram Rao, E. (2021). Atmospheric cold pools and their influence on sea surface temperature in the Bay of Bengal. *Journal of Geophysical Research: Oceans*, *126*(9). https://doi.org/10.1029/2021JC017297

Girishkumar, M. S., Joseph, J., Thangaprakash, V. P., Pottapinjara, V., & McPhaden, M. J. (2017). Mixed layer temperature Budget for the northward propagating summer monsoon intraseasonal oscillation (MISO) in the central Bay of Bengal. *Journal of Geophysical Research: Oceans*, *122*(11), 8841–8854. https://doi.org/10.1002/2017JC013073

Girishkumar, M. S., Ravichandran, M., McPhaden, M. J., & Rao, R. R. (2011). Intraseasonal variability in barrier layer thickness in the south central Bay of Bengal. *Journal of Geophysical Research*, *116*(3), C03009. https://doi.org/10.1029/2010JC006657

Hamza, V., & Babu, C. A. (2007). Boundary Layer Characteristics associated with sea breeze circulation over Cochin. *Mausam*, *58*(1), 75–86. https://doi.org/10.54302/mausam.v58i1.1134

Hersbach, H., Bell, B., Berrisford, P., Hirahara, S., Horanyi, A., Munoz-Sabater, J., et al. (2020). The ERA5 global reanalysis [Dataset]. Quarterly Journal of the Royal Meteorological Society, *146*(730), 1999–2049. https://doi.org/10.1002/qj.3803

Hill, C. M., Fitzpatrick, P. J., Corbin, J. H., Lau, Y. H., & Bhate, S. K. (2010). Summertime precipitation regimes associated with the sea breeze and land Breeze in southern Mississippi and eastern Louisiana. *Weather and Forecasting*, *25*(6), 1755–1779. https://doi.org/10.1175/2010WAF2222340.1

Jena, B. K., Anuraj, K. S., Suseentharan, V., Tushar, K., & Karthikeyan, T. (2019). Indian coastal ocean radar network. *Current Science*, *116*(3), 372–378. https://doi.org/10.18520/cs/v116/i3/372-378

Jiang, X., & Li, J. (2011). Influence of the annual cycle of sea surface temperature on the monsoon onset. *Journal of Geophysical Research*, *116*(D10), D10105. https://doi.org/10.1029/2010JD015236

Jofia, J., Girishkumar, M. S., McPhaden, M. J., & Pattabhi Ram Rao, E. (2021). Diurnal variability of atmospheric cold pool events and associated air-sea interactions in the Bay of Bengal during the summer monsoon. *Climate Dynamics*, *56*, 837–853. https://doi.org/10.1007/s00382-020-05506-w

Johnson, R. H., & Ciesielski, P. E. (2017). Multiscale variability of the atmospheric boundary layer during DYNAMO. *Journal of the Atmospheric Sciences*, *74*(12), 4003–4021. https://doi.org/10.1175/jas-d-17-0182.1

Joseph, J., Girishkumar, M. S., McPhaden, M. J., & Rao, E. P. R. (2021). Diurnal variability of atmospheric cold pool events and associated air-sea interactions in the Bay of Bengal during the summer monsoon. *Climate Dynamics*, *56*(3–4), 837–853. https://doi.org/10.1007/S00382-020-05506-W

Kilpatrick, T., Xie, S. P., & Nasuno, T. (2017). Diurnal convection-wind coupling in the Bay of Bengal. *Journal of Geophysical Research: Atmospheres*, *122*(18), 9705–9720. https://doi.org/10.1002/2017JD027271

Kolukula, S. S., Baduru, B., Murty, P. L. N., Kumar, J. P., Rao, E. P. R., & Shenoi, S. S. C., (2020). Gaps filling in HF radar sea surface current data using complex empirical orthogonal Functions [Dataset]. Pure and Applied Geophysics, *177* (12), 5969–5992. https://doi.org/10.1007/S00024-020-02613-x

Masselink, G., & Pattiaratchi, C. B. (2001). Characteristics of the sea breeze system in Perth, Western Australia, and its effect on the nearshore wave climate. *Journal of Coastal Research*, *17*(1), 173–187. Retrieved from http://www.jstor.org/stable/4300161

McPhaden, M. J., Meyers, G., Ando, K., Masumoto, Y., Murty, V. S. N., Ravichandran, M., et al. (2009). RAMA: The research moored Array for African–Asian–Australian monsoon analysis and prediction. *Bulletin of the American Meteorological Society*, *90*(4), 459–480. https://doi.org/10.1175/2008BAMS2608.1

Miller, S. T. K., & Keim, B. D. (2003). Synoptic-scale controls on the sea breeze of the central New England coast. *Weather and Forecasting*, *18*(2), 236–248. https://doi.org/10.1175/1520-0434(2003)018<0236:scotsb>2.0.co;2

Miller, S. T. K., Keim, B. D., Talbot, R. W., & Mao, H. (2003). Sea breeze: Structure, forecasting, and impacts. *Reviews of Geophysics*, *41*(3), 1011. https://doi.org/10.1029/2003RG000124

Mujumdar, M., Salunke, K., Rao, S. A., Ravichandran, M., & Goswami, B. N. (2011). Diurnal cycle induced amplification of sea surface temperature intraseasonal oscillations over the Bay of Bengal in summer monsoon season. *IEEE Geoscience and Remote Sensing Letters*, *8*(2), 206–210. https://doi.org/10.1109/LGRS.2010.2060183

Neetu, S., Shetye, S., & Chandramohan, P. (2006). Impact of sea breeze on wind-seas off Goa, west coast of India. *Journal of Earth System Science*, *115*(2), 229–234. https://doi.org/10.1007/BF02702036

Orlic, M. (2011). Wind-induced currents directed to the left of the wind in the northern hemisphere: An elementary explanation and its historical background. *Geofizika*, *28*, 219–228.

Pielke, R. A. (1973). A three-dimensional numerical model of the sea breezes over south Florida. *Monthly Weather Review*, *102*(2), 115–139. https://doi.org/10.1175/1520-0493(1974)102<0115:atdnmo>2.0.co;2

Porson, A., Steyn, D. G., & Schayes, G. (2007). Formulation of an index for sea breezes in opposing winds. *Journal of Applied Meteorology and Climatology*, *46*(8), 1257–1263. https://doi.org/10.1175/jam2525.1

Prasad, T. G. (2004). A comparison of mixed-layer dynamics between the Arabian Sea and Bay of Bengal: One-dimensional model results. *Journal of Geophysical Research*, *109*(C3), C03035. https://doi.org/10.1029/2003JC002000

Praveen Kumar, B., Cronin, M. F., Joseph, S., Ravichandran, M., & Sureshkumar, N. (2017). Latent heat flux sensitivity to sea surface temperature: Regional Perspectives. *Journal of Climate*, *30*(1), 129–143. https://doi.org/10.1175/JCLI-D-16-0285.1

Rafiq, S., Pattiaratchi, C., & Janeković, I. (2020). Dynamics of the land–sea breeze system and the surface current response in South-West Australia. *Journal of Marine Science and Engineering*, *8*(11), 1–28. https://doi.org/10.3390/jmse8110931

Rani, S. I., Ramachandran, R., Subrahamanyam, D. B., Alappattu, D. P., & Kunhikrishnan, P. K. (2010). Characterization of sea/land breeze circulation along the west coast of Indian sub-continent during pre-monsoon season. *Atmospheric Research*, *95*(4), 367–378. https://doi.org/10.1016/J.ATMOSRES.2009.10.009

Rao, R. R., & Sivakumar, R. (2000). Seasonal variability of near-surface thermal structure and heat budget of the mixed layer of the tropical Indian Ocean from a new global ocean temperature climatology. *Journal of Geophysical Research*, *105*(C1), 995–1016. https://doi.org/10.1029/1999jc900220

Rao, R. R., & Sivakumar, R. (2003). Seasonal variability of sea surface salinity and salt budget of the mixed layer of the north Indian Ocean. *Journal of Geophysical Research*, *108*(C1), 9-1. https://doi.org/10.1029/2001JC000907

Rudnick, D. L., & Weller, R. A. (1993). Observations of superinertial and near-inertial wind-driven flow. *Journal of Physical Oceanography*, *23*(11), 2351–2359. https://doi.org/10.1175/1520-0485(1993)023<2351:oosani>2.0.co;2

Samanta, D., Hameed, S. N., Jin, D., Thilakan, V., Ganai, M., Rao, S. A., & Deshpande, M. (2018). Impact of a narrow coastal Bay of Bengal sea surface temperature front on an Indian summer monsoon simulation. *Scientific Reports*, *8*(1), 1–12. https://doi.org/10.1038/s41598-018-35735-3

Sengupta, D., & Ravichandran, M. (2001). Oscillations of Bay of Bengal sea surface temperature during the 1998 summer monsoon. *Geophysical Research Letters*, *28*(10), 2033–2036. https://doi.org/10.1029/2000GL012548

Seo, H., Subramanian, A. C., Miller, A. J., & Cavanaugh, N. R. (2014). Coupled impacts of the diurnal cycle of sea surface temperature on the Madden–Julian oscillation. *Journal of Climate*, *27*(22), 8422–8443. https://doi.org/10.1175/JCLI-D-14-00141.1

Shenoi, S. S. C., Shankar, D., & Shetye, S. R. (2002). Differences in heat budgets of the near-surface Arabian Sea and Bay of Bengal: Implications for the summer monsoon. *Journal of Geophysical Research*, *107*(C6), 3052_1–3052_14. https://doi.org/10.1029/2000jc000679

Shetye, S. R., Gouveia, A. D., Shankar, D., Shenoi, S. S. C., Vinayachandran, P. N., Sundar, D., et al. (1996). Hydrography and circulation in the western Bay of Bengal during the northeast monsoon. *Journal of Geophysical Research*, *101*(C6), 14011–14025. https://doi.org/10.1029/95JC03307

Short, E., Vincent, C. L., & Lane, T. P. (2019). Diurnal cycle of surface winds in the maritime continent observed through satellite scatterometry. *Monthly Weather Review*, *147*(6), 2023–2044. https://doi.org/10.1175/MWR-D-18-0433.1

Srivastava, A., Dwivedi, S., & Mishra, A. K. (2018). Investigating the role of air-sea forcing on the variability of hydrography, circulation, and mixed layer depth in the Arabian Sea and Bay of Bengal. *Oceanologia*, *60*(12), 169–186. https://doi.org/10.1016/j.oceano.2017.10.001

Stull, R. B. (1988). An introduction to boundary layer meteorology. In *An introduction to boundary layer meteorology*. https://doi.org/10.1007/978-94-009-3027-8

Thadathil, P., Muraleedharan, P. M., Rao, R. R., Somayajulu, Y. K., Reddy, G. V., & Revichandran, C. (2007). Observed seasonal variability of barrier layer in the Bay of Bengal. *Journal of Geophysical Research*, *112*(C2), C02009. https://doi.org/10.1029/2006JC003651

Thangaprakash, V. P., Girishkumar, M. S., Suprit, K., Suresh Kumar, N., Chaudhuri, D., Dinesh, K., et al. (2016). What controls seasonal evolution of sea surface temperature in the Bay of Bengal?: Mixed layer heat budget analysis using moored buoy observations along 90°E. *Oceanography*, *29*(2), 202–213. https://doi.org/10.5670/OCEANOG.2016.52

Turk, F. J., Hristova-Veleva, S., & Giglio, D. (2021). Examination of the daily cycle wind vector modes of variability from the constellation of microwave scatterometers and radiometers. *Remote Sensing*, *13*(1), 141. https://doi.org/10.3390/rs13010141

Ueyama, R., & Deser, C. (2008). A climatology of diurnal and semidiurnal surface wind variations over the tropical Pacific Ocean based on the tropical atmosphere ocean moored buoy array. *Journal of Cimate*, *21*(4), 593–607. https://doi.org/10.1175/jcli1666.1

Venkatesan, R., Shamji, V. R., Latha, G., Mathew, S., Rao, R. R., Muthiah, A., & Atmanand, M. A. (2013). In situ ocean subsurface time-series measurements from OMNI buoy network in the Bay of Bengal. *Current Science*, *104*(9), 1166–1177.

Webster, P. J., Bradley, E. F., Fairall, C. W., Godfrey, J. S., Hacker, P., Houze, R. A., et al. (2002). The JASMINE Pilot study. *Bulletin of the American Meteorological Society*, *83*(11), 1603–1630. https://doi.org/10.1175/BAMS-83-11-1603

Weller, R. A., Farrar, J. T., Buckley, J., Mathew, S., Venkatesan, R., Lekha, J. S., et al. (2016). Air-sea interaction in the Bay of Bengal. *Oceanography*, *29*(2), 28–37. https://doi.org/10.5670/OCEANOG.2016.36

Weller, R. A., Farrar, J. T., Seo, H., Prend, C., Sengupta, D., Sree Lekha, J., et al. (2019). Moored observations of the surface meteorology and air-sea fluxes in the northern Bay of Bengal in 2015. *Journal of Climate*, *32*(2), 549–573. https://doi.org/10.1175/JCLI-D-18-0413.1

Wentz, F. J., Scott, J., Hoffman, R., Leidner, M., Atlas, R., & Ardizzone, J. (2015). Remote sensing systems cross-calibrated multi-platform (CCMP) 6-hourly ocean vector wind analysis product on 0.25 deg grid, version 2.0 [Dataset]. Remote Sensing Systems, Santa Rosa, CA. Retrieved from http://www.remss.com/measurements/ccmp

Wermter, J., Noble, S., & Viner, B. (2022). Impacts of the thermal gradient on inland advecting sea breezes in the southeastern United States. *Atmosphere*, *13*(7), 1004. https://doi.org/10.3390/atmos13071004

Wexler, R. (1946). Theory and observations of land and sea breezes. *Bulletin of the American Meteorological Society*, *27*(6), 272–287. https://doi.org/10.1175/1520-0477-27.6.272

Wielicki, B. A., Barkstrom, B. R., Harrison, E. F., Lee, R. B., Smith, G. L., & Cooper, J. E. (1996). Clouds and the Earth's Radiant Energy System (CERES): An earth observing system experiment [Dataset]. *Bulletin of the American Meteorological Society*, *77*(5), 853–868. https://doi.org/10.1175/1520-0477(1996)077<0853:CATERE>2.0.CO;2

Woodson, C. B., Eerkes-Medrano, D. I., Flores-Morales, A., Foley, M. M., Henkel, S. K., Hessing-Lewis, M., et al. (2007). Local diurnal upwelling driven by sea breezes in northern Monterey Bay. *Continental Shelf Research*, *27*(18), 2289–2302. https://doi.org/10.1016/J.CSR.2007.05.014

Yu, L., Jin, X., & Weller, R. A. (2007). Annual, seasonal, and interannual variability of air–sea heat fluxes in the Indian ocean. *Journal of Climate*, *20*(13), 3190–3209. https://doi.org/10.1175/JCLI4163.1

Zhu, L., Meng, Z., Zhang, F., & Markowski, P. M. (2017). The influence of sea- and land-breeze circulations on the diurnal variability in precipitation over a tropical island. *Atmospheric Chemistry and Physics*, *17*(21), 13213–13232. https://doi.org/10.5194/ACP-17-13213-2017